



# Synergistic effect of single-atom Ag and hierarchical tremella-like g-C<sub>3</sub>N<sub>4</sub>: Electronic structure regulation and multi-channel carriers transport for boosting photocatalytic performance

Linlin Sun<sup>a</sup>, Yibing Feng<sup>a</sup>, Kai Ma<sup>b</sup>, Xiaohan Jiang<sup>a</sup>, Zhengyang Gao<sup>b</sup>, Jigang Wang<sup>a,c,\*</sup>, Nan Jiang<sup>d,\*\*</sup>, Xiaoshuo Liu<sup>b,\*\*</sup>

<sup>a</sup> Jiangsu key Laboratory of Advanced Metallic Materials, School of Materials Science and Engineering, Southeast University, Nanjing 211189, PR China

<sup>b</sup> School of Energy and Power Engineering, North China Electric Power University, Baoding 071003, PR China

<sup>c</sup> Xizang Engineering Laboratory for Water Pollution Control and Ecological Remediation, Xizang Minzu University, Xianyang 712082, PR China

<sup>d</sup> Collaborative Innovation Center for Cardiovascular Disease, Translational Medicine of Jiangsu, School of Pharmacy, Nanjing Medical University, Nanjing 211166, PR China

## ARTICLE INFO

### Keywords:

Synergetic effect  
Charge transfer behavior  
Tremella-like g-C<sub>3</sub>N<sub>4</sub>  
Single-atom silver  
Photocatalytic

## ABSTRACT

It is significant to realize the synergistic effect of single-atom sites and its support to obtain excellent performance photocatalysts. Here, single-atom silver (SAAg) is embedded into the hierarchical tremella-like carbon nitride (3DT-CN) by an efficient one-step reduction method. The photo-degradation mechanism of SAAg/3DT-CN for tetracycline (TC) is first proposed. And the synergistic effect to improve photocatalytic activity is also discussed in depth. Density functional theory (DFT) calculations and physicochemical characterizations reveal that the synergistic effect of SAAg and 3DT-CN has improved the absorption capacity of visible light, the binding energy with oxygen, charge transfer behavior and other properties. Electron spin resonance (ESR) and capture experiments validate the active species involved in the reaction. The first-order kinetic constant of TC degradation by SAAg/3DT-CN is 8.4 times and 3.8 times that of 3DT-CN and AgNP/3DT-CN in 75 min, respectively. This work provides a meritorious structure-activity strategy for the removal of refractory antibiotics.

## 1. Introduction

Antibiotics are commonly used in medical treatment, animal husbandry, veterinary medicine, and other fields. The researches manifest that approximately 90% of underutilized antibiotics are released into the environment. Currently, tetracycline antibiotics have been detected in groundwater, surface water and other water environments with an average concentration of more than 17 ng/L [1–6]. The concentration of tetracycline (TC) in some rivers has even reached 497 ng/L in China [7]. Correspondingly, problems with drug-resistant bacteria, chronic toxic effects and enrichment in food chains have appeared. Since the sustainable development of ecosystems is essential for survival and even low concentrations of antibiotics can also affect the balance of ecosystems, it is significant to find an effective strategy for removing the residual antibiotics existing in the environment [8–11]. Semiconductor

photocatalysis technology has attracted much attention because of its advantages, such as being renewable, clean, economical, and so on [12, 13]. Specifically, the inexhaustible sunshine of green environmental protection serves as the driving force, and semiconductors assist as photocatalysts. Semiconductors are excited to produce electrons (e<sup>-</sup>) and holes (h<sup>+</sup>) that can lead to the formation of active species covering •O<sub>2</sub><sup>-</sup>, •OH as well as h<sup>+</sup>, and subsequently resulting in the organic pollutants degradation, when the energy of sunlight is greater than or equal to the band gap energy of semiconductors [14–16]. Therefore, it is significant to research and apply a suitable band gap semiconductor photocatalyst for the photo-gradation of organic pollutants including antibiotics, especially tetracycline.

Graphite carbon nitride (g-C<sub>3</sub>N<sub>4</sub>), a nonmetallic polymer semiconductor material, has a suitable band gap (~2.7 eV). In addition, g-C<sub>3</sub>N<sub>4</sub> possesses the advantages of excellent thermochemical stability,

\* Corresponding author at: Jiangsu key Laboratory of Advanced Metallic Materials, School of Materials Science and Engineering, Southeast University, Nanjing 211189, PR China.

\*\* Corresponding authors.

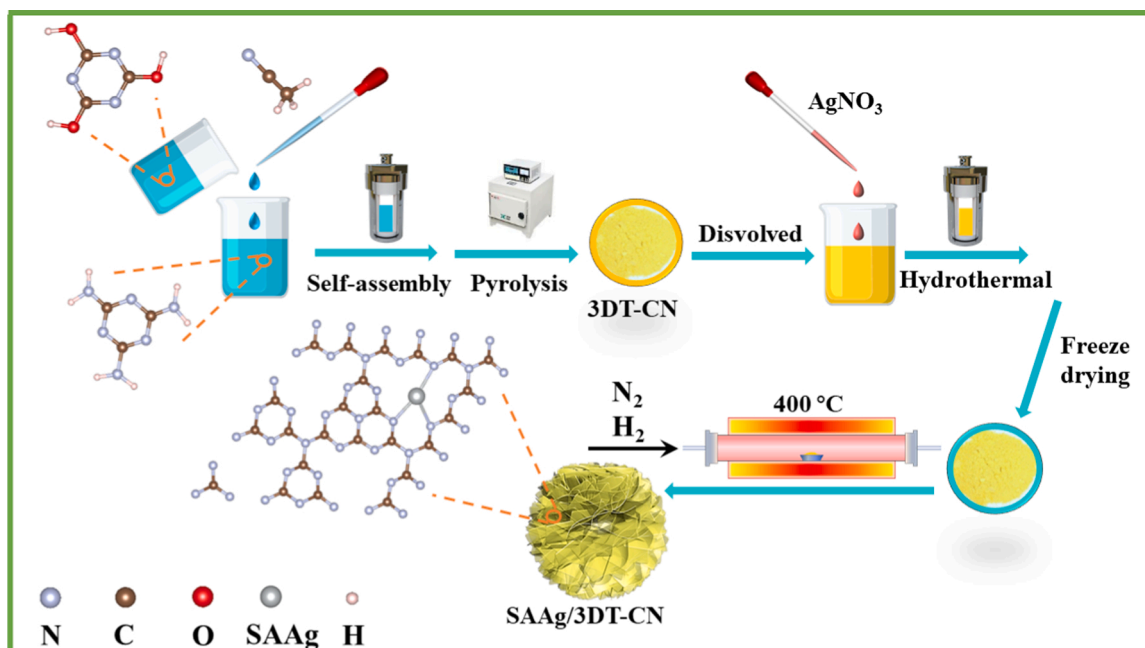
E-mail addresses: [wangjigang@seu.edu.cn](mailto:wangjigang@seu.edu.cn) (J. Wang), [jiangnan@njmu.edu.cn](mailto:jiangnan@njmu.edu.cn) (N. Jiang), [liuxiaoshuo@ncepu.edu.cn](mailto:liuxiaoshuo@ncepu.edu.cn) (X. Liu).

<https://doi.org/10.1016/j.apcatb.2022.121106>

Received 12 November 2021; Received in revised form 22 December 2021; Accepted 14 January 2022

Available online 20 January 2022

0926-3373/© 2022 Elsevier B.V. All rights reserved.



**Scheme 1.** Schematic illustration of the formation process of SAAg/3DT-CN.

environmental affinity and economic value and has attracted widespread attention. However, the original g-C<sub>3</sub>N<sub>4</sub> has some deficiencies, such as low electron conductivity, fast carrier recombination behavior and relatively few surface-active sites [17–19]. It is worth noting that some modification strategies aiming to improve photocatalytic activity have been attempted. Nanostructure engineering, heterojunction structure and single-atom engineering have emerged to effectively solve these problems and improve the photocatalytic performance of g-C<sub>3</sub>N<sub>4</sub>. Nanostructured engineering, such as nanoribbons, nanorods, nanotubes, nanosheets and so on, has been shown to enhance photocatalytic activity. However, the aggregation problem of nano-catalysts and recombination of photo-generated carriers are often encountered in the as-prepared g-C<sub>3</sub>N<sub>4</sub> [20]. To solve these problems, the construction of a hierarchical g-C<sub>3</sub>N<sub>4</sub> structure seems to be an effective and feasible strategy. Recently, Moradi et al. [21] developed g-C<sub>3</sub>N<sub>4</sub> nanosheets to achieve effective photocatalytic removal of amoxicillin. Song et al. [22] constructed ultralong hollow chain-ball-like g-C<sub>3</sub>N<sub>4</sub> and effectively inhibited the recombination of photo-generated carriers. Dang et al. [23] prepared fractionally hollow phosphorus doped g-C<sub>3</sub>N<sub>4</sub> microspheres, which increased the absorption range of light and accelerated charge transfer. Due to the special hierarchical structure, the reflection and scattering of sunlight can be achieved, consequently resulting in the enhancement of the light capture capability via more transmission channels. Accordingly, it is necessary to develop a kind of g-C<sub>3</sub>N<sub>4</sub> with hierarchical structure morphology.

In addition, the heterojunction structure can improve the charge separation around the interface of the photocatalysts, but it cannot be applied to perfect the internal electron transport in g-C<sub>3</sub>N<sub>4</sub> [24,25]. Moreover, the atoms existing on the surface of the nanoparticle are limited during participation in the reaction and other responses. It has been found that monatomic engineering can regulate the internal electrons of g-C<sub>3</sub>N<sub>4</sub> at the atomic scale and maximize the utilization of metals [26]. To date, some monatomic metal/g-C<sub>3</sub>N<sub>4</sub> nano-composites have been prepared with excellent performance. Yang et al. [27] successfully prepared Au monatomic on amino-modified g-C<sub>3</sub>N<sub>4</sub> with remarkable CO<sub>2</sub> reduction properties. Yang et al. [28] proposed implanting monoatomic cobalt in g-C<sub>3</sub>N<sub>4</sub> to provide a green and efficient material for photocatalytic degradation of oxytetracycline. Jiang et al. [29] constructed single-atom silver in g-C<sub>3</sub>N<sub>4</sub> catalyst with a novel

structure that exhibited excellent catalytic activity and durability for efficient photocatalytic hydrogen evolution. Single-atom Ag is anchored on g-C<sub>3</sub>N<sub>4</sub>, which not only extends the visible light absorption region but also facilitates electron transfer [30–32]. g-C<sub>3</sub>N<sub>4</sub> contains an extremely high content of nitrogen atoms, and single metal atoms are uniformly anchored on the network by forming coordination bonds with lone pair electrons of the nitrogen. Specifically, the silver atoms dispersed in g-C<sub>3</sub>N<sub>4</sub> can accelerate the charge separation through chemical bonding, significantly improving the photocatalytic activity [33]. However, we note that there are few studies on the synergistic application of g-C<sub>3</sub>N<sub>4</sub> photocatalysts with the introduction of single-atom Ag to the photocatalytic degradation of antibiotics. Besides, for the synthesis of monatomic metal composited g-C<sub>3</sub>N<sub>4</sub>, a multistep synthesis process or the preparation of complex precursors is usually needed. Therefore, the optimization and application of facile synthesis and the discussion on the synergistic effect of g-C<sub>3</sub>N<sub>4</sub> and monatomic silver still need to be further explored.

Herein, single-atom Ag incorporating the hierarchical structure of the 3DT-CN photocatalyst is prepared by an efficient one-step reduction method. Interestingly, the hierarchical tremella-like structure of 3DT-CN provides more active sites and transport channels for the reaction and enhances the light harvesting ability through multiple reflections and scattering. SAAg regulates the internal electrons of 3DT-CN and maximizes the utilization of the metal. Moreover, the utilization of electronic structure mutation is proven. Density functional theory (DFT) investigations demonstrate that the synergistic effect of SAAg and 3DT-CN directly improves the charge density distribution and carrier transport efficiency of the photocatalyst. The results of photocatalytic experiments demonstrate that the SAAg/3DT-CN photocatalyst has good catalytic performance, even higher than AgNP/3DT-CN. The steady-state photoluminescence and time-resolved photoluminescence illustrate that the introduction of SAAg accelerates the dissociation of excitons. Moreover, we obtain profound insight into the synergistic reaction mechanism of SAAg/3DT-CN on TC, charge transfer and separation behavior, and the generation of active species and so on. Therefore, the positive effects endow the SAAg/3DT-CN photocatalyst with excellent photocatalytic activity and good stability.

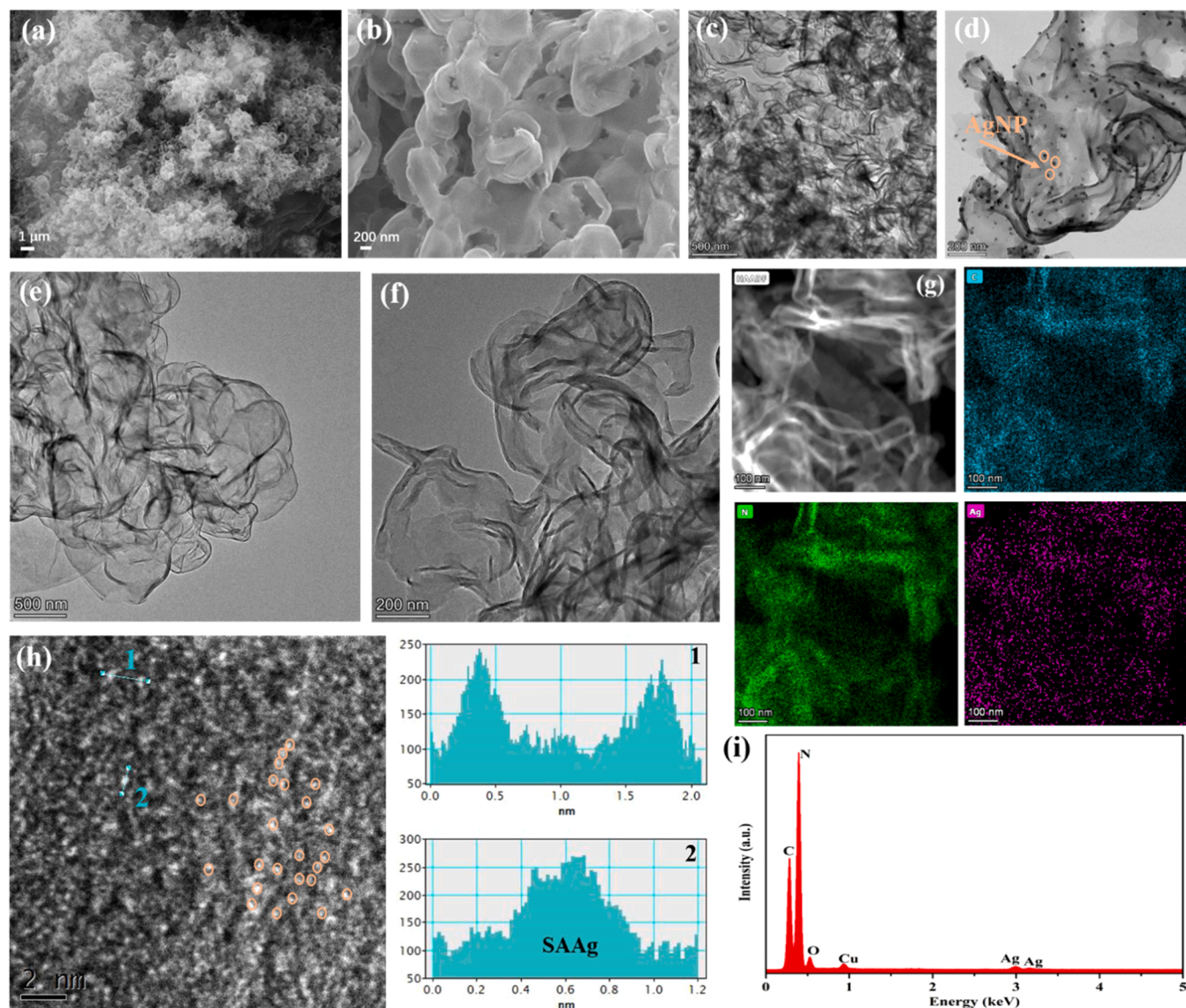


**Fig. 1.** (a, b) SEM images of 3DT-CN; TEM images of (c) 3DT-CN, (d) AgNP/3DT-CN and (e, f) SAAg/3DT-CN; (g) HAADF-STEM with elemental mapping of SAAg/3DT-CN; (h) AC-HAADF-STEM and (i) EDS images of SAAg/3DT-CN.

## 2. Experimental section

### 2.1. Chemicals and materials

Melamine ( $C_3H_6N_6$ ), cyanuric acid ( $C_3H_3N_3O_3$ ), 5,5-dimethyl-1-pyrroline N-oxide ( $C_6H_{11}NO$ ), ascorbic acid ( $C_6H_8O_6$ ), isopropanol ( $C_3H_8O$ ), ethylenediaminetetraacetic acid disodium ( $C_{10}H_{14}N_2Na_2O_8$ ) and catalase (CAT, 2000–5000 U/mg protein) were purchased from Aladdin Reagent. Silver nitrate ( $AgNO_3$ ), sodium sulfate ( $Na_2SO_4$ ), ethanol ( $C_2H_5OH$ ), acetonitrile ( $C_2H_3N$ ) and tetracycline ( $C_{22}H_{24}N_2O_8$ ) were supplied by Sinopharm Chemical Reagent. Nitrogen ( $N_2$ ) and hydrogen ( $H_2$ ) were provided by Zhongput Gas Co., Ltd. The standard grade of all reagents was analytical grade without further purification and deionized water was supplied by a local water purification company.

### 2.2. Materials preparation

#### 2.2.1. Synthesis of three-dimensional tremella-like carbon nitride (3DT-CN)

Three-dimensional tremella-like carbon nitride (3DT-CN) was

prepared by one-step thermal polymerization process.  $C_3H_6N_6$  and  $C_3H_3N_3O_3$  were self-assembled for 4 h in a solution of deionized water, ethyl alcohol, and acetonitrile (molar ratio=2:2:1) to achieve uniformly mixed solution. The morphology of g- $C_3N_4$  was controlled by adding the amount of acetonitrile. Then, the mixed solution was transferred to an autoclave (12 h, 110 °C) and then centrifuged (washed three times with deionized water and ethanol) and dried (60 °C, 8 h) to obtain supramolecular samples. The supramolecule was finely ground into powder as the reaction precursor. Subsequently, the precursor was calcinated at 550 °C for 4 h at a flow rate of 2.3 °C/min to obtain yellow product. It was carefully ground to produce a yellow powder known as 3DT-CN.

#### 2.2.2. Synthesis of single-atom silver dispersed 3DT-CN (SAAg/3DT-CN) and Ag nanoparticles modified 3DT-CN (AgNP/3DT-CN)

The SAAg/3DT-CN material was prepared by an efficient one-step reduction process. 3DT-CN (0.2 g) was fully dispersed in 120 mL of water and then a certain amount of aqueous  $AgNO_3$  (0.1 M) was added drop by drop. After 6 h of full reaction in a magnetic stirrer, the  $Ag^+$  ions were uniformly dispersed in the 3DT-CN to obtain the reactant. The reactant was transferred to an autoclave (50 mL, 110 °C) for 12 h. Afterwards, the solution was freeze-dried, and then the obtained specimen

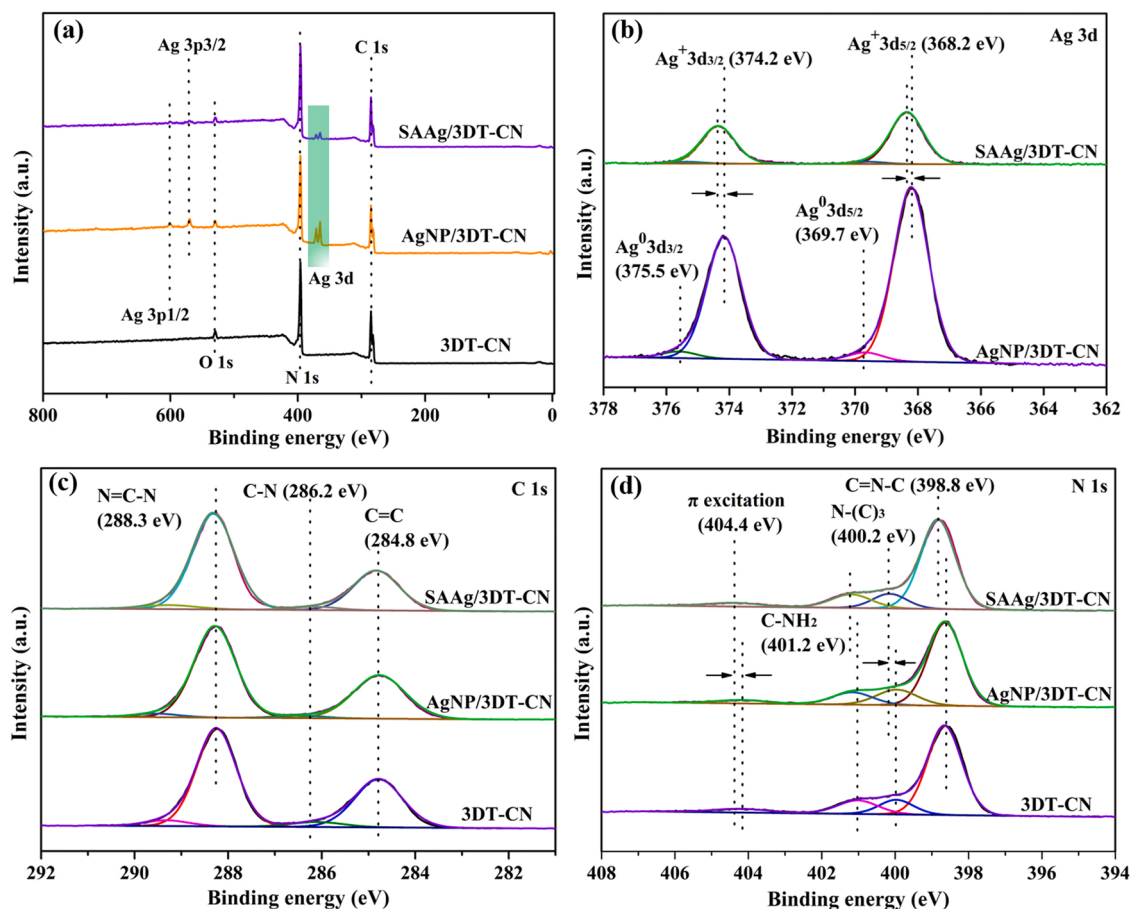


Fig. 2. XPS spectra of 3DT-CN, AgNP/3DT-CN and SAAg/3DT-CN. (a) Full survey; (b) Ag 3d; (c) C 1 s and (d) N 1 s.

was fully ground to produce a powder. The powder was loaded into a ceramic ark and calcined into a mixed gas atmosphere ( $V(N_2):V(H_2) = 18:2$ ) at  $400^\circ\text{C}$  to obtain the target product (SAAg/3DT-CN). The content of SAAg in the SAAg/3DT-CN material is 2.65 wt%, according to inductively coupled plasma emission spectrometry (ICP) results. A schematic illustration of the formation process of SAAg/3DT-CN is shown in Scheme 1. AgNP/3DT-CN was synthesized by the same steps without the introduction of  $N_2$  and  $H_2$  when the products were calcinated.

### 2.3. Device characterization

The details of physicochemical characterizations, photoelectrochemical tests, and density functional theory (DFT) calculations are provided in the supporting information (SI).

### 2.4. Performance evaluation and reproducibility experiments

The photodegradation of TC was used to evaluate the photocatalytic activity of 3DT-CN, AgNP/3DT-CN and SAAg/3DT-CN under visible light irradiation. Briefly, the as-prepared photocatalysts (50 mg) were dispersed into TC solution (20 mg/L, 200 mL) in a cylindrical reactor. The circulate water around the reactor was used to make the reaction at a constant temperature. The suspension was continuously stirred for 30 min under dark conditions to reach adsorption/desorption equilibrium, and then a xenon lamp ( $\lambda \geq 420\text{ nm}$ ) was employed to irradiate the reactants for 2 h. The reaction products were taken every 15 min and the absorbance was immediately measured at a wavelength of 357 nm by UV-vis spectrophotometry after centrifugation. To ensure the accuracy of the experimental results, the average value of three

measurements was selected. The test results are proven within a certain error range by using error bars. After the above steps, the photocatalyst was collected, washed, and dried, and then the cycle experiment was carried out by the same steps.

## 3. Results and discussion

### 3.1. Morphology and microstructure analysis

The morphologies of the as-prepared samples were investigated by scanning electron microscopy (SEM) and transmission electron microscopy (TEM). As shown in Fig. 1a-b, 3DT-CN exhibits three-dimensional tremella-like features by the assembly of irregular nanosheets. The microstructure of 3DT-CN measured by TEM (Fig. 1c) corresponds with the SEM results. At the same time, one can find that the specimen seems to be transparent, indicating that the specimen is quite thin, which benefits achieving a larger surface. Fig. 1d shows the morphology of AgNP/3DT-CN. Those black dots uniformly dispersed on 3DT-CN, partially marked with orange circles, are Ag nanoparticles. In contrast, for the SAAg/3DT-CN specimen, although the 3DT-CN matrix has the same morphology, no black dots can be found in Fig. 1e, and a further magnified morphology is shown in Fig. 1f. Meanwhile, HAADF-STEM with elemental mapping images (Fig. 1g) verifies that the C, N and Ag elements are uniformly dispersed throughout SAAg/3DT-CN. Due to the limitation of the detection sensitivity of the common TEM apparatus, it is quite difficult to obtain the morphology of a single atom. Based on the comprehensive analysis of the morphologies and element detection, one can deduce that the existing form of silver in SAAg/3DT-CN is not nanoparticles and it could be a single atom.

To confirm the incorporation scale of silver elements, Aberration-

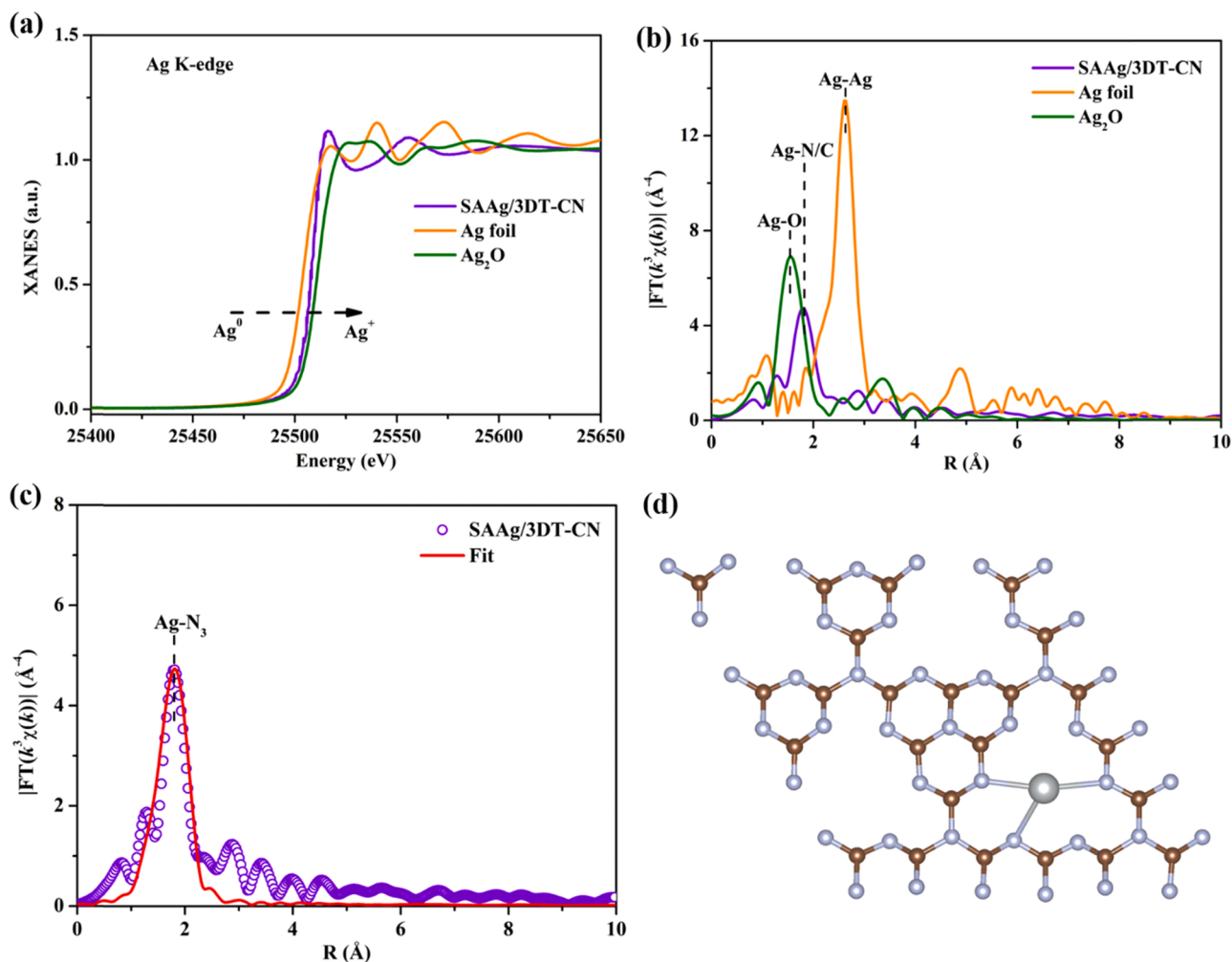


Fig. 3. (a) Ag K-edge XANES profiles and (b) EXAFS spectra of SAAg/3DT-CN, Ag foil and Ag<sub>2</sub>O samples; (c) The Ag K-edge R space EXAFS fitting results of SAAg/3DT-CN; (d) Schematic illustration of the Ag-N<sub>3</sub> moiety structure.

Corrected High-Angle Annular Dark Field STEM (AC-HAADF-STEM) was also employed to investigate the specimen. The AC-HAADF-STEM image (Fig. 1h) of SAAg/3DT-CN exhibits bright dots, which means single-atom Ag, illustrating that SAAg was successfully obtained. The intensity distribution analysis of the spherical aberration electron microscope image is further confirmed along line 1 and line 2 that the white spots in the image are indeed SAAg. In particular, SAAg is evenly dispersed and no aggregation of Ag clusters is found. As demonstrated by EDS (energy dispersive spectrometry) in Fig. 1i, silver element is successfully loaded in 3DT-CN with a content of 2.59 wt%, which is consistent with ICP. Specific amounts of each element are presented in Table S1. The Cu peak is caused by TEM grid material. Since SAAg has been incorporated in 3DT-CN at the atomic scale, some special effects and excellent performances are worthy of investigation.

### 3.2. Surface chemical state and structure analysis

The surface elemental compositions and chemical states of 3DT-CN, AgNP/3DT-CN and SAAg/3DT-CN were measured by X-ray photoelectron spectroscopy (XPS). From the survey spectrum (Fig. 2a), the elements (C, N, O and Ag) of SAAg/3DT-CN are detected, indicating the successful introduction of silver elements compared with 3DT-CN. According to the survey spectrum analysis, the mass ratio of SAAg is 2.74% (Table S2) which is consistent with ICP. Due to the different yields of SAAg/3DT-CN and AgNP/3DT-CN, signal peaks of different intensities are detected at the locations of Ag. However, the performance of SAAg/

3DT-CN is still expected to be higher than that of AgNP/3DT-CN which will be demonstrated in the following section. Furthermore, the high-resolution details of Ag 3d are analyzed in Fig. 2b. The typical characteristic peaks at 368.2 eV and 374.2 eV are depicted, attributing to the binding energies of Ag 3d<sub>5/2</sub> and Ag 3d<sub>3/2</sub>, respectively. Specifically, the two pairs of peaks at 368.2/374.2 eV and 369.7/375.5 eV can be assigned to Ag<sup>+</sup> and Ag<sup>0</sup>, respectively. Whereas, the Ag 3d of SAAg/3DT-CN shifts to a higher binding energy than that of AgNP/3DT-CN. It is evident that the oxidation state of Ag for SAAg/3DT-CN is between Ag<sup>+</sup> and metal Ag<sup>0</sup> [17,34], which is consistent with the positive valence (+0.658) calculated by DFT calculations. The location mismatch of the Ag<sup>0</sup> peaks reconfirms that there is no metallic silver aggregation in the SAAg/3DT-CN [35]. The C 1s spectrum (Fig. 2c) possesses three peaks at 288.3, 286.2, and 284.8 eV, corresponding to sp<sup>2</sup>-hybridized carbon (N-C=N), sp<sup>3</sup>-coordinated carbon (C-N) and graphitic species (C=C), respectively [36,37]. The C=N-C (398.8 eV), N-(C)<sub>3</sub> (400.2 eV), C-NH<sub>2</sub> (401.2 eV) and  $\pi$  excitation (404.4 eV) of SAAg/3DT-CN are detected and shift 0.3, 0.2, 0.3 and 0.2 eV to higher binding energies in N 1s spectrum (Fig. 2d) [38,39]. Furthermore, the transfer of lone electron pairs between N and Ag by the Ag-N coordination bond triggers the shift of the N-(C)<sub>3</sub> peak towards a higher binding energy. The typical peak of the O 1s spectrum (Fig. S1) is attributed to C-O (532.1 eV) and O-H (533.4 eV) bonds, respectively [40].

To further elucidate the successful synthesis and coordination environment of SAAg, the characterizations of X-ray absorption near edge structure (XANES) and extended X-ray absorption fine structure

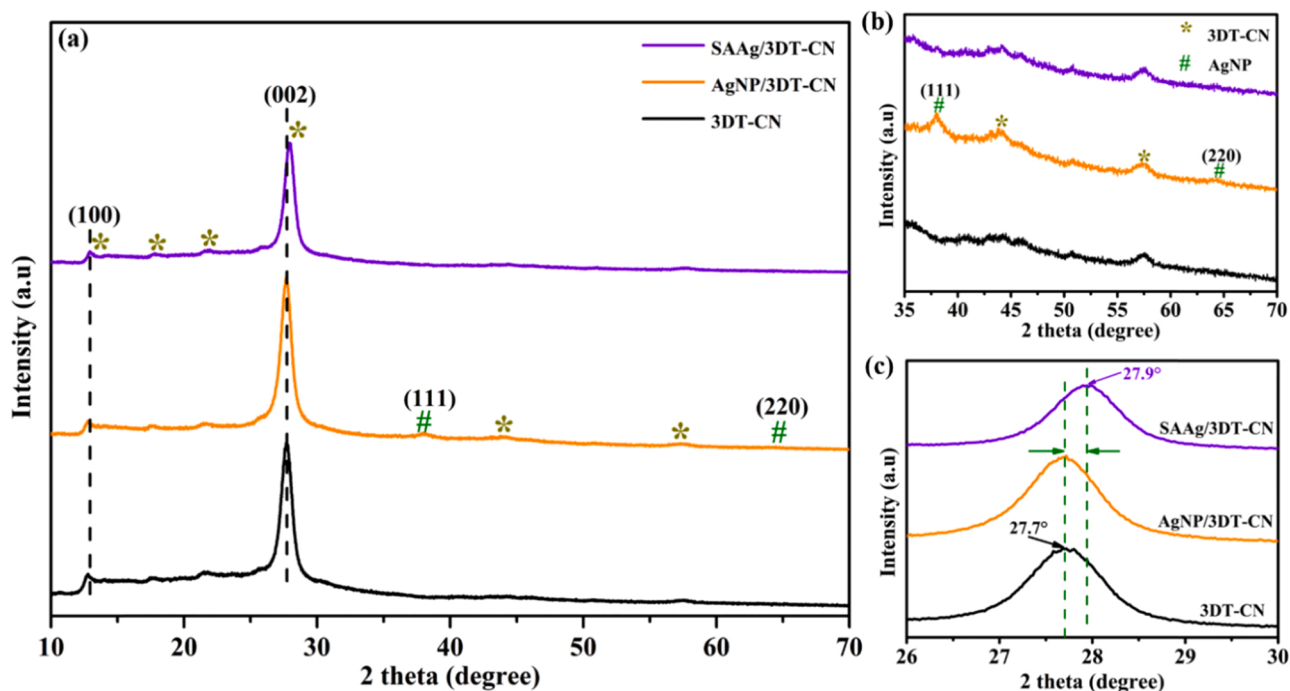


Fig. 4. The XRD patterns of (a) 3DT-CN, AgNP/3DT-CN and SAAg/3DT-CN and (b, c) exhibit an enlarged version.

(EXAFS) were carried out. The near-edge feature of SAAg/3DT-CN converts to higher energies relative to Ag foil and the absorption threshold is located between Ag foil and the reference  $\text{Ag}_2\text{O}$  in the Ag K-edge spectra (Fig. 3a). It is easy to determine that the oxidation state of SAAg in SAAg/3DT-CN is between 0 and 1 due to the strong interaction between SAAg and 3DT-CN, which agrees with the DFT calculation result. As shown in Fig. 3b, Ag foil and  $\text{Ag}_2\text{O}$  exhibit strong characteristic peaks at positions of 2.62 Å and 1.54 Å, which can be attributed to Ag-Ag and Ag-O bonds, respectively. Obviously, the presence of these two peaks is not detected in SAAg/3DT-CN, which proves that SAAg is successfully prepared. In addition, a characteristic peak of Ag-N/C is detected in SAAg/3DT-CN. In order to quantitatively reveal the coordination environment around SAAg, the least square EXAFS fitting curve is presented in Fig. 3c, where the fitting curve (red line) has a good match with the experimental data (purple circles). The data obtained by the analysis of fitting results demonstrate that the coordination number of SAAg/3DT-CN is 3 and then SAAg coordinate with three N atoms in

the triazine unit structure of 3DT-CN (denoted as Ag-N<sub>3</sub> sites). The relevant structure diagram is presented in Fig. 3d. In addition, the average bond length of Ag-N is 2.37 Å. More details about the EXAFS fitting structure parameters of SAAg/3DT-CN are presented in Table S3.

X-ray diffraction (XRD) was used to characterize the crystalline structure of the as-prepared samples. 3DT-CN exhibits two main characteristic peaks at the positions of 12.8° and 27.7° that are attributed to the (100) and (002) diffraction planes in Fig. 4a. Similarly, the XRD patterns indicate that 3DT-CN has typical tri-s-triazine units and a conjugated aromatic structure [41,42]. Fig. 4b-c show an enlarged version of the part of as-prepared samples (3DT-CN, AgNP/3DT-CN and SAAg/3DT-CN). Notably, two new peaks are detected at 38.1° and 64.3° in AgNP/3DT-CN (Fig. 4b), corresponding to the (111) and (220) planes of Ag nanoparticles. This result is consistent with the position of the standard peak on the standard card (JCPDS: 01-089-3722) [43,44]. As can be seen from Fig. 4, 3DT-CN and AgNP/3DT-CN have the same crystal structure. It shows that the introduction of silver nanoparticles

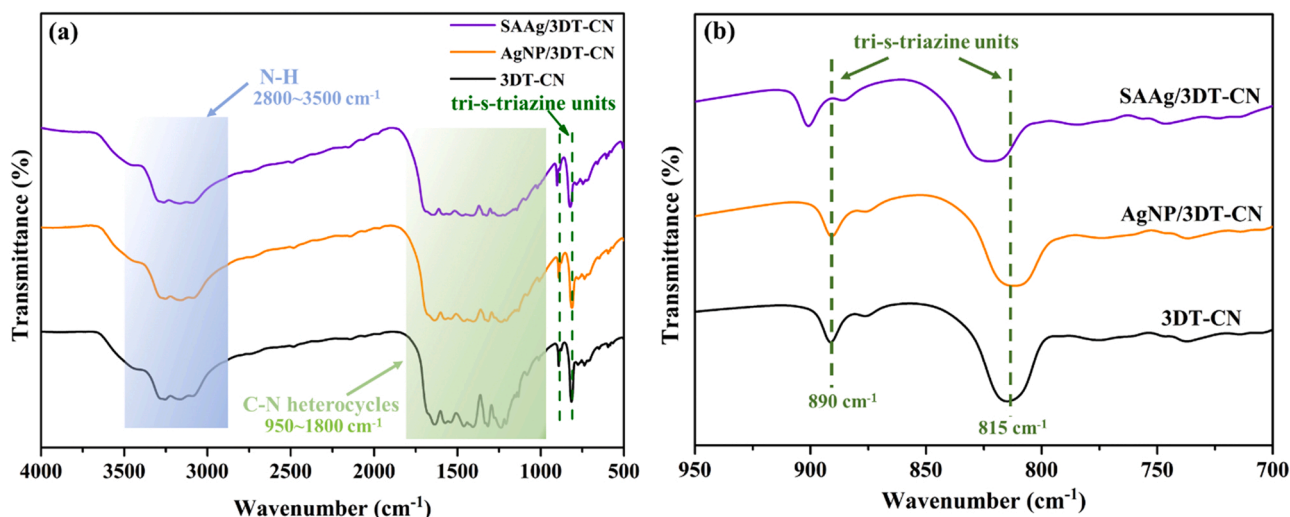
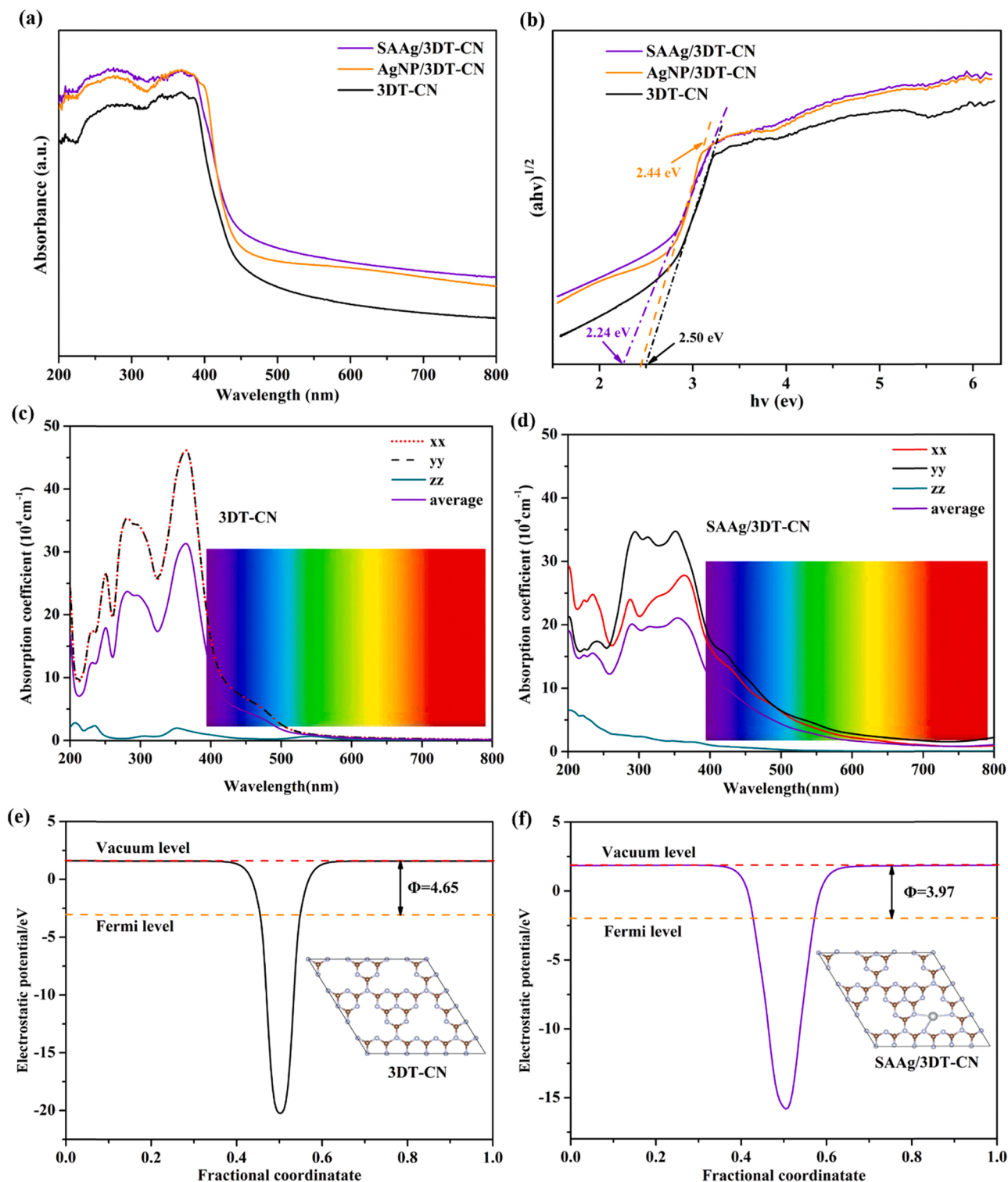


Fig. 5. FT-IR spectra of (a) 3DT-CN, AgNP/3DT-CN and SAAg/3DT-CN and the (b) exhibits an enlarged version.



**Fig. 6.** (a) UV-vis DRS and (b) Tauc plots of 3DT-CN, AgNP/3DT-CN and SAAg/3DT-CN; (c,d) the light absorption coefficient and (e,f) work function of 3DT-CN and SAAg/3DT-CN by DFT calculations.

does not change the crystal structure of 3DT-CN. Significantly, no peak of Ag nanoparticles is detected in SAAg/3DT-CN. In comparison with 3DT-CN, the peak intensities of the (100) and (002) crystal faces are slightly reduced, attributing to the deformation of the plane structure around the Ag atoms center in SAAg/3DT-CN [45,46]. And the (002) peak of SAAg/3DT-CN is shifted from  $27.7^\circ$  to  $27.9^\circ$  (Fig. 4c). According to Bragg's law, the layer distance of SAAg/3DT-CN is reduced, which indicates an enhanced interaction between single-atom Ag and

heptazine units. The peaks of 3DT-CN and Ag nanoparticles are marked by asterisks (\*) and well signs (#) in Fig. 4, respectively.

In order to confirm the change in the functional groups structure of the as-prepared materials, Fourier transform infrared (FT-IR) spectra are presented in Fig. 5. It infers that the peaks are located at  $2800\text{--}3500 \text{ cm}^{-1}$  (highlighted by the blue shaded regions) in Fig. 5a, corresponding to the N-H stretching vibrations of 3DT-CN. The C-N heterocycle stretching vibrations at  $950\text{--}1800 \text{ cm}^{-1}$  (highlighted by the

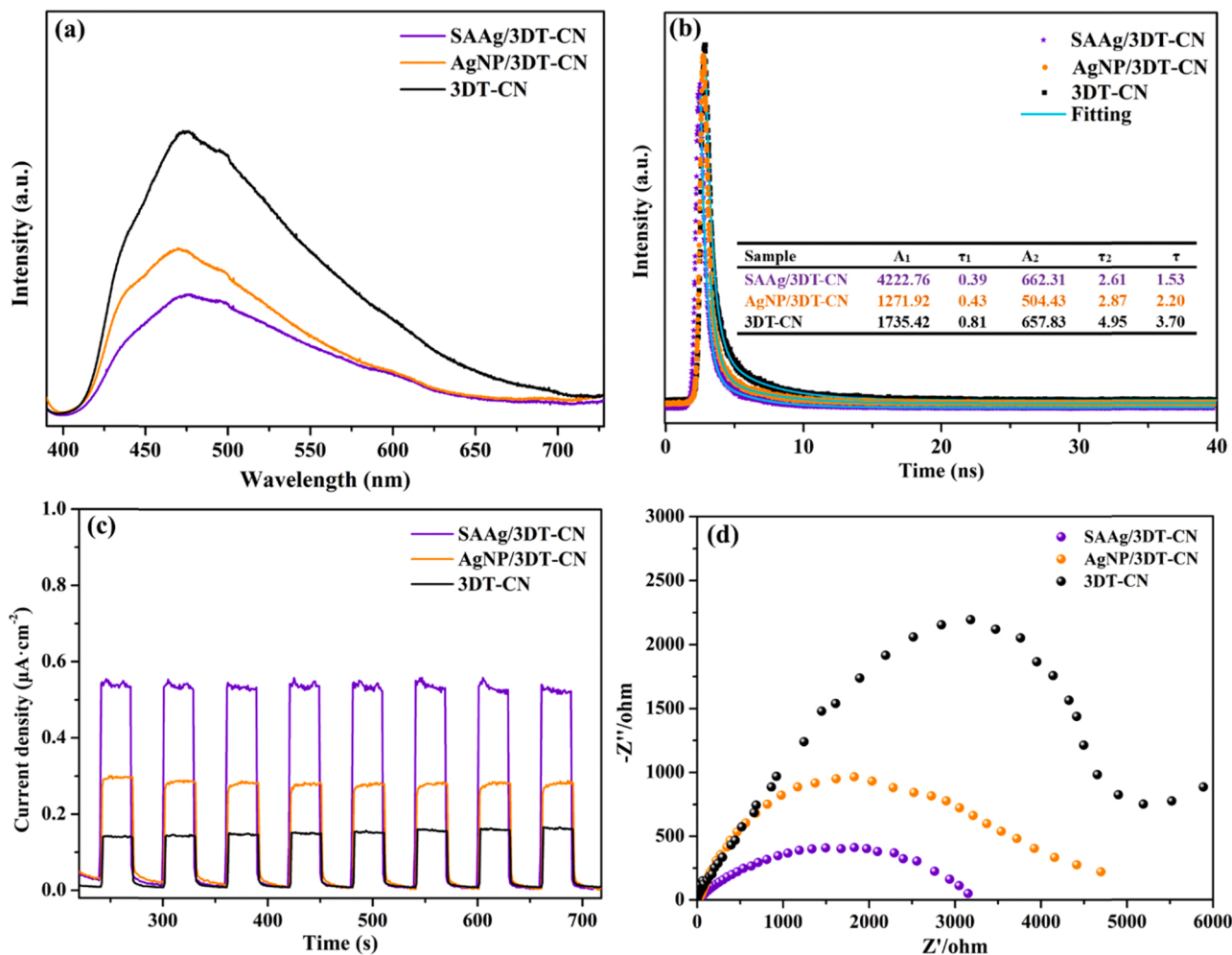


Fig. 7. (a) PL spectra, (b) TR-PL decay curves, (c) transient photocurrent responses and (d) Nyquist plots of 3DT-CN, AgNP/3DT-CN and SAAg/3DT-CN.

green shaded regions) indicate the existence of a polymeric melon network in the as-prepared samples [47–49]. Whereas, the C-N heterocycle peaks of SAAg/3DT-CN progressively decreased, indicating that SAAg may bond to C-N heterocycles, particularly C-NH<sub>2</sub> sites [50]. Attentionally, the tensile vibration of the C-N heterocycles shifts to a higher frequency region, possibly due to an increase in the force constant of the C-N heterocycles [51]. In addition, two characteristic peaks appear at 890 cm<sup>-1</sup> and 815 cm<sup>-1</sup>, which are attributed to the stretching vibration of the tri-s-triazine units. The characteristic peak of tri-s-triazine units is magnified in Fig. 5b, and the spectral line is obviously shifted to a high wavenumber. It indicates that single-atom Ag is successfully introduced and interacts with the tri-s-triazine units. 3DT-CN and AgNP/3DT-CN display similar spectra, implying that the stretching vibration mode of the functional groups does not change after the introduction of Ag nanoparticles.

### 3.3. Optical and photoelectrochemical properties

Efficient light absorption capacity can make full use of solar energy, generating more photogenerated electron-hole pairs to participate in the redox reaction. Thus, it is necessary to extend the light absorption range [52,53]. The UV-Vis DRS spectra of 3DT-CN, AgNP/3DT-CN and SAAg/3DT-CN were measured and are shown in Fig. 6. The absorption of AgNP/3DT-CN in the visible (Vis) light region (Fig. 6a) was attributed to the localized surface plasmon resonance (LSPR) of Ag nanoparticles [54,55]. The intrinsic absorption edge of SAAg/3DT-CN manifests a significant redshift compared with that of 3DT-CN and AgNP/3DT-CN.

Thus, SAAg/3DT-CN extends the Vis light absorption range, and then more electrons and holes can be produced and applied to the photocatalytic reaction. In addition, the absorption spectrum of SAAg/3DT-CN exhibits the highest light absorption intensity in the Vis region, thereby more carriers are generated under Vis light irradiation [35,56]. Concretely, SAAg incorporated 3DT-CN can improve Vis light utilization. The band gap energies ( $E_g$ ) of 3DT-CN, AgNP/3DT-CN and SAAg/3DT-CN are plotted according to the Kubelka-Munk theory in Fig. 6b. The  $E_g$  of SAAg/3DT-CN is narrowed by 0.26 eV due to the intromission of SAAg into the framework of 3DT-CN. It is inferred that lower energies are necessary for the electronic transition from the valence band maximum (VBM) to the conduction band minimum (CBM) [27].

Density functional theory (DFT) calculations are performed to shed light on the intrinsic properties of SAAg/3DT-CN and 3DT-CN with the calculation details accessible in Section 3 of the SI. We find that the absorption rate is increased at 600–780 nm after the introduction of SAAg (Fig. 6c-d), demonstrating that the embedded SAAg in the 3DT-CN lattice extends the Vis light absorption range and subsequently benefits an increase in the photocatalytic performance. In addition, the work function ( $\Phi$ ), representing the minimum energy that must be provided for an electron to escape immediately from the catalyst surface, is also provided in our work. According to the definition, the work function is calculated by Eq. (1) [57].

$$\phi = E_{\text{vac}} - E_f \quad (1)$$

Where,  $E_f$  and  $E_{\text{vac}}$  are the potentials of the Fermi level and vacuum

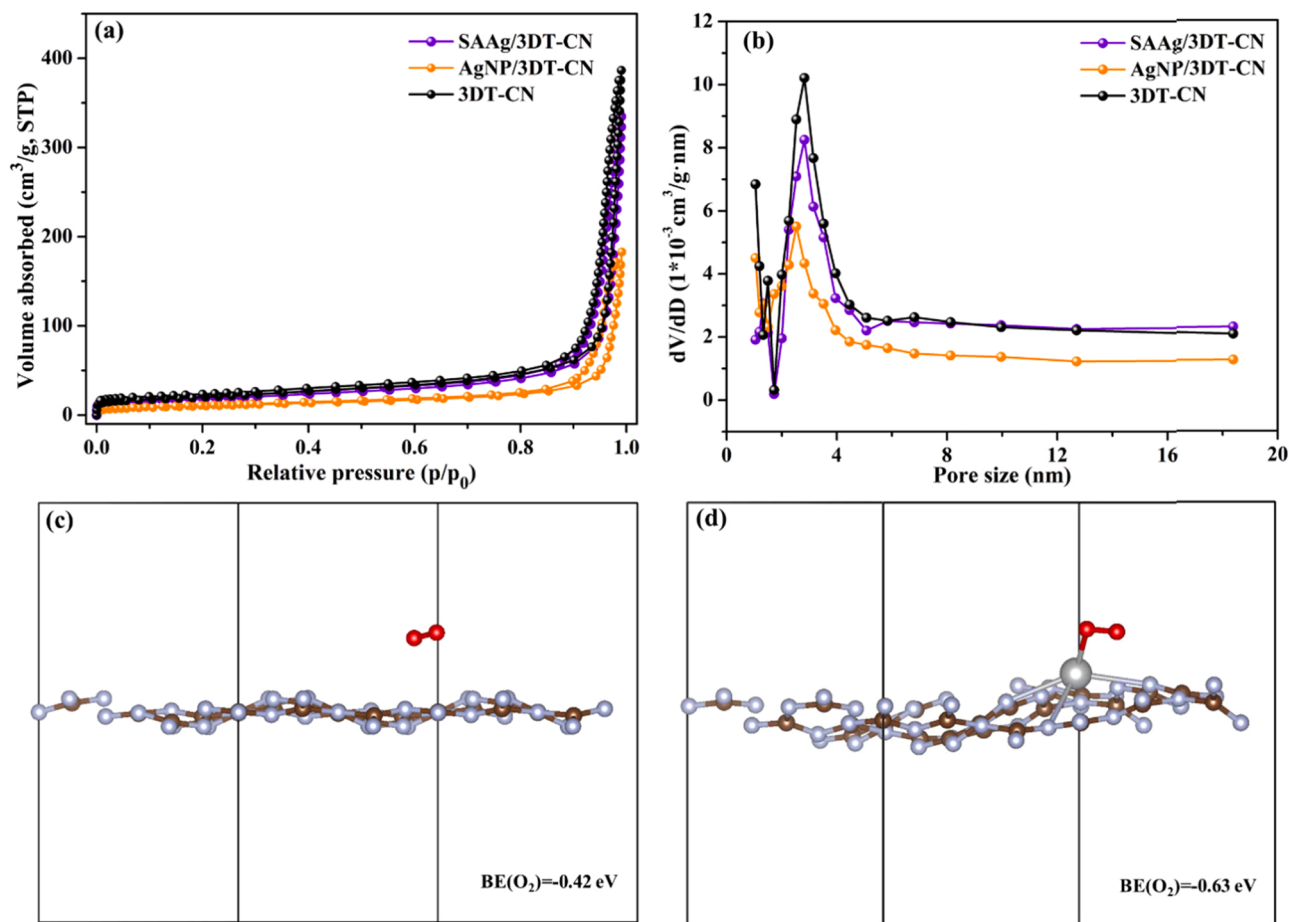


**Fig. 8.** (a) N<sub>2</sub> adsorption-desorption isotherms and (b) pore size distribution curves of 3DT-CN, AgNP/3DT-CN and SAAg/3DT-CN; (c) the binding energy (BE) of 3DT-CN and (d) SAAg/3DT-CN to O<sub>2</sub>.

level, respectively. As shown in Fig. 6e, the calculated work function of 3DT-CN is 4.65 eV, which is consistent with the previous work [58]. With the introduction of SAAg, the Fermi energy level rises and the work function of SAAg/3DT-CN decreases to 3.97 eV (Fig. 6f), making it easier for the electrons in SAAg/3DT-CN to escape, and a higher concentration of photogenerated electrons can be produced.

The charge separation and transfer efficiency are a significant influencing factors in the process of photocatalysis. To measure the charge transfer efficiency and the lifetimes of photo-generated carriers, the steady-state photoluminescence (PL) spectra and time-resolved photoluminescence (TR-PL) spectra excited at 390 nm of 3DT-CN, AgNP/3DT-CN and SAAg/3DT-CN are presented in Fig. 7. As displayed in Fig. 7a, the PL intensity of SAAg/3DT-CN has an obvious decrease compared with 3DT-CN and AgNP/3DT-CN. Specifically, charge transfer is limited for poor mesosphere, while the introduction of SAAg changes the original lamellar structure providing new channels for charge transfer [53,59]. Thereby, the monatomic doping of Ag effectively inhibits the recombination of photo-generated carriers. The emission peak of SAAg/3DT-CN at 470 nm is redshifted, attributing the charge transfer between 3DT-CN and SAAg. The TR-PL attenuation curves are enumerated in Fig. 7b. Besides, the fitting data are fitted biexponentially using Eq. (2) [60].

$$R(t) = A_1 \exp\left(-\frac{t}{\tau_1}\right) + A_2 \exp\left(-\frac{t}{\tau_2}\right) \quad (2)$$

Where,  $\tau_1$ ,  $\tau_2$ ,  $A_1$  and  $A_2$  represent the values of lifetime and the amplitudes of the normalized decay component, respectively. The average lifetime ( $\tau_{ave}$ ) is calculated by Eq. (3) [61].

$$\tau_{ave} = \frac{A_1 \tau_1^2 + A_2 \tau_2^2}{A_1 \tau_1 + A_2 \tau_2} \quad (3)$$

The charge average lifetime (1.53 ns) of SAAg/3DT-CN is much shorter than that of 3DT-CN (3.70 ns) and AgNP/3DT-CN (2.20 ns), illustrating that some effective electron transfer channels might be formed between 3DT-CN and SAAg and consequently benefit rapid exciton dissociation in SAAg/3DT-CN [62,63]. Specifically, AAg is embedded in 3DT-CN, and a built-in electric field is induced to drive the migration of photoexcited electrons from the outermost layer of 3DT-CN. Meanwhile, nonradiative channels are also opened to promote effective charge transfer by virtue of Ag-N bonding states [64,65].

In addition, the charge migration behaviors are also investigated by photoelectrochemical experiments, and the details of the tests are presented in Section 2 of the SI. The photocurrent intensity presents a steady trend after several cycles. As depicted in Fig. 7c, the transient photocurrent response intensity of SAAg/3DT-CN is 0.55  $\mu\text{A}\cdot\text{cm}^{-2}$ , which is approximately 3.93 and 1.96 times that of 3DT-CN (0.14  $\mu\text{A}\cdot\text{cm}^{-2}$ ) and AgNP/3DT-CN (0.28  $\mu\text{A}\cdot\text{cm}^{-2}$ ), respectively. The enhanced current density of SAAg/3DT-CN indicates that SAAg has excellent light-harvesting ability. Thus, SAAg/3DT-CN has enhanced charge separation efficiency and accelerated charge transfer rate [66]. Moreover, electrochemical impedance spectroscopy (EIS) was performed to obtain the charge migration ability (Fig. 7d). The EIS Nyquist radius of SAAg/3DT-CN sharply decreases, indicating that SAAg/3DT-CN has a smaller charge transfer resistance at the interface of the electrolyte solution than 3DT-CN and AgNP/3DT-CN [67]. That is, SAAg embedded on 3DT-CN promotes efficient photocarrier migration properties. Therefore, SAAg/3DT-CN has excellent charge separation

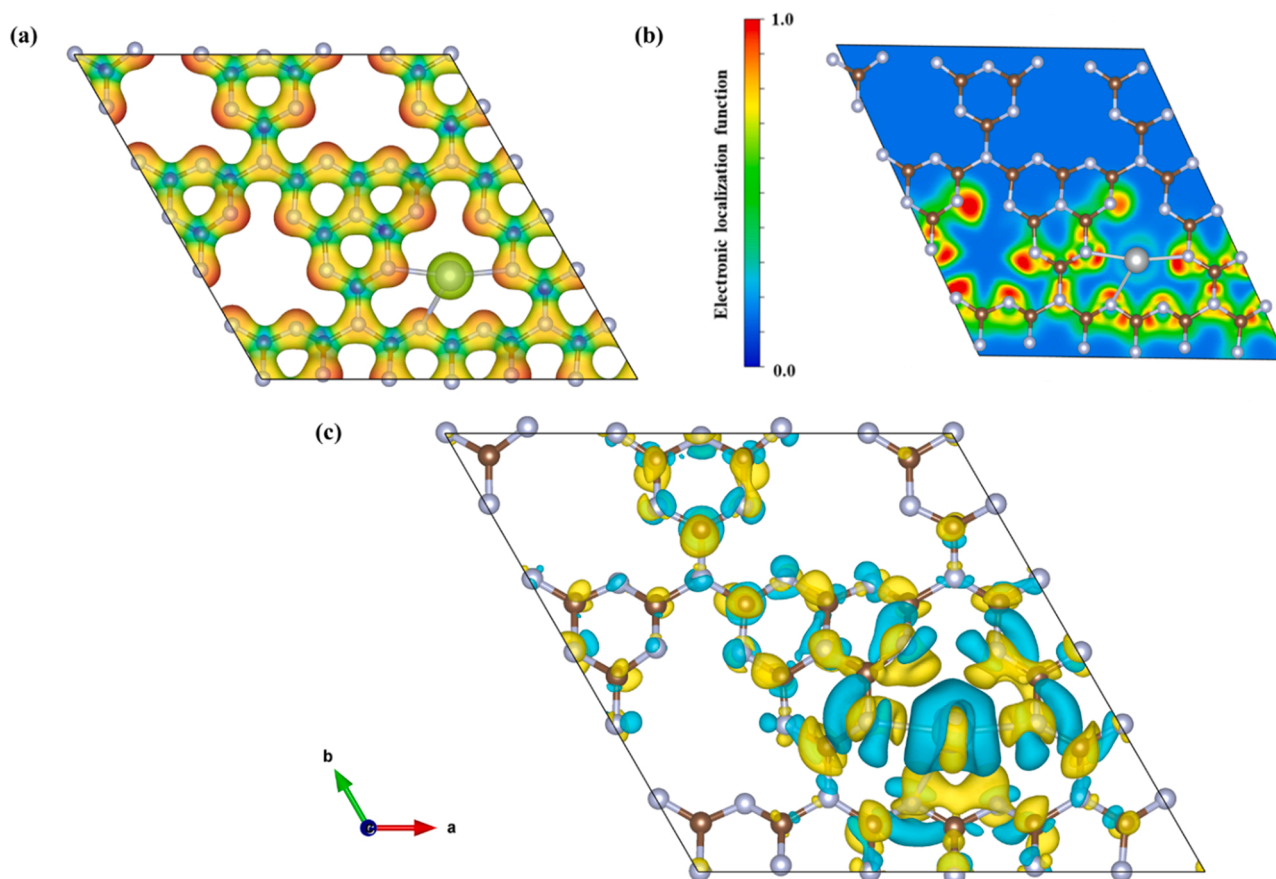


Fig. 9. (a) ESP of SAAg/3DT-CN with an isosurface of  $0.02 \text{ e/Bohr}^3$ ; (b) ELF of SAAg/3DT-CN and (c) EDD of SAAg/3DT-CN with an isosurface of  $0.01 \text{ e/Å}^3$ .

efficiency for the photocatalytic action of TC by the above analysis.

The  $\text{N}_2$  adsorption-desorption isotherms and pore size distribution curves (Fig. 8) of the as-prepared samples were studied by the BET method. The curves show typical IV with  $\text{H}_3$  hysteresis rings indicating the existence of mesopores in Fig. 8a. The relevant data are presented in Table S4. 3DT-CN shows a high specific surface area ( $91.106 \text{ m}^2\cdot\text{g}^{-1}$ ), which is attributed to the hierarchical structure by self-assembly. The specific surface area of SAAg/3DT-CN ( $87.207 \text{ m}^2\cdot\text{g}^{-1}$ ) is similar to that of 3DT-CN. It indicates that the introduction of SAAg did not affect the reduction of active sites and the establishment of hierarchical structure. Although the BET of SAAg/3DT-CN is slightly smaller than that of SAAg/3DT-CN, the photocatalytic performance of SAAg/3DT-CN (part 3.5 in the back) is obviously higher than that of 3DT-CN due to the synergistic effect of SAAg and 3DT-CN. However, the specific surface area of AgNP/3DT-CN ( $57.004 \text{ m}^2\cdot\text{g}^{-1}$ ) is significantly decreased, which may be caused by some nanoparticles occupying part of the surface area of 3DT-CN or pore blocking. The pore size distribution further confirms the rich pore structure of 3DT-CN and SAAg/3DT-CN throughout the mesoporous range (Fig. 8b). Therefore, the hierarchical 3DT-CN constructs mesoporous channels, provides more active sites for interface redox reactions, and accelerates the mass transfer kinetics of reactants [68,69]. Moreover, the binding energy (BE) is one of the most important quantities to evaluate binding strength. It is calculated to evaluate the binding of  $\text{O}_2$  on catalysts, and the deformation energy, which corresponds to the monomer geometry distortion because of the formation of complexes, is ignored to better present intrinsic binding between monomers inside a complex without this component. As shown in Fig. 8c-d, the BE of oxygen molecules of SAAg/3DT-CN ( $-0.63 \text{ eV}$ ) is calculated and it is larger than that of 3DT-CN ( $-0.42 \text{ eV}$ ), suggesting that embedded SAAg promotes the combination of  $\text{O}_2$  [70]. The combination of more  $\text{O}_2$  promotes the electron transfer of SAAg/3DT-CN to

$\text{O}_2$ , producing more active species during the catalytic reaction.

### 3.4. Regulating effect on electronic structure

Since changes in the microscopic electronic structure play a significant role in the improvement of macroscopic photochemical, physical, and optical properties, the electrostatic potential (ESP), electronic localization function (ELF), and electron density difference (EDD) of SAAg/3DT-CN were used to analyze the electronic structures. As shown in Fig. 9a-b, ESP and ELF demonstrate that lone pair electrons exist on pyridine nitrides in 3DT-CN. In comparison to the traditional (or undoped)  $\text{g-C}_3\text{N}_4$  composed of periodic arrayed tri-s-triazine units, the EDD result (Fig. 9c) indicates that the single-atom Ag embedded in the structure of tri-s-triazine units results in a perturbation in the conjugated aromatic system. Namely, due to the “catfish effect”, the embedded SAAg causes the relative enrichment of electrons in the 3DT-CN substance, subsequently leading to the improvement of electron migration or transmission ability. The higher density of the electron cloud between the local electric fields of Ag and N atoms there is, the higher of electrons transmission ability between SAAg and 3DT-CN there will be, thus benefitting in the inhibition of the carrier recombination [71,72].

The calculated band structures of pure monolayer  $\text{g-C}_3\text{N}_4$  and single-atom Ag catalysts at the GGA-PBE level are given in Fig. S5. The band structure indicates that  $\text{g-C}_3\text{N}_4$  is an indirect bandgap semiconductor with a band gap value of  $1.19 \text{ eV}$  at the GGA-PBE level, which is consistent with the reported literature ( $1.20 \text{ eV}$ ) [73]. Due to the limitations of the PBE functional, novel calculations using the HSE06 hybrid functional with high levels were carried out. As shown in Fig. 10a-b, the calculated bandgaps of monolayer  $\text{g-C}_3\text{N}_4$  and SAAg/3DT-CN are  $2.77 \text{ eV}$  and  $2.37 \text{ eV}$ , which correspond well to the experimental results ( $2.50 \text{ eV}$  and  $2.24 \text{ eV}$ ), respectively. Compared to 3DT-CN, the

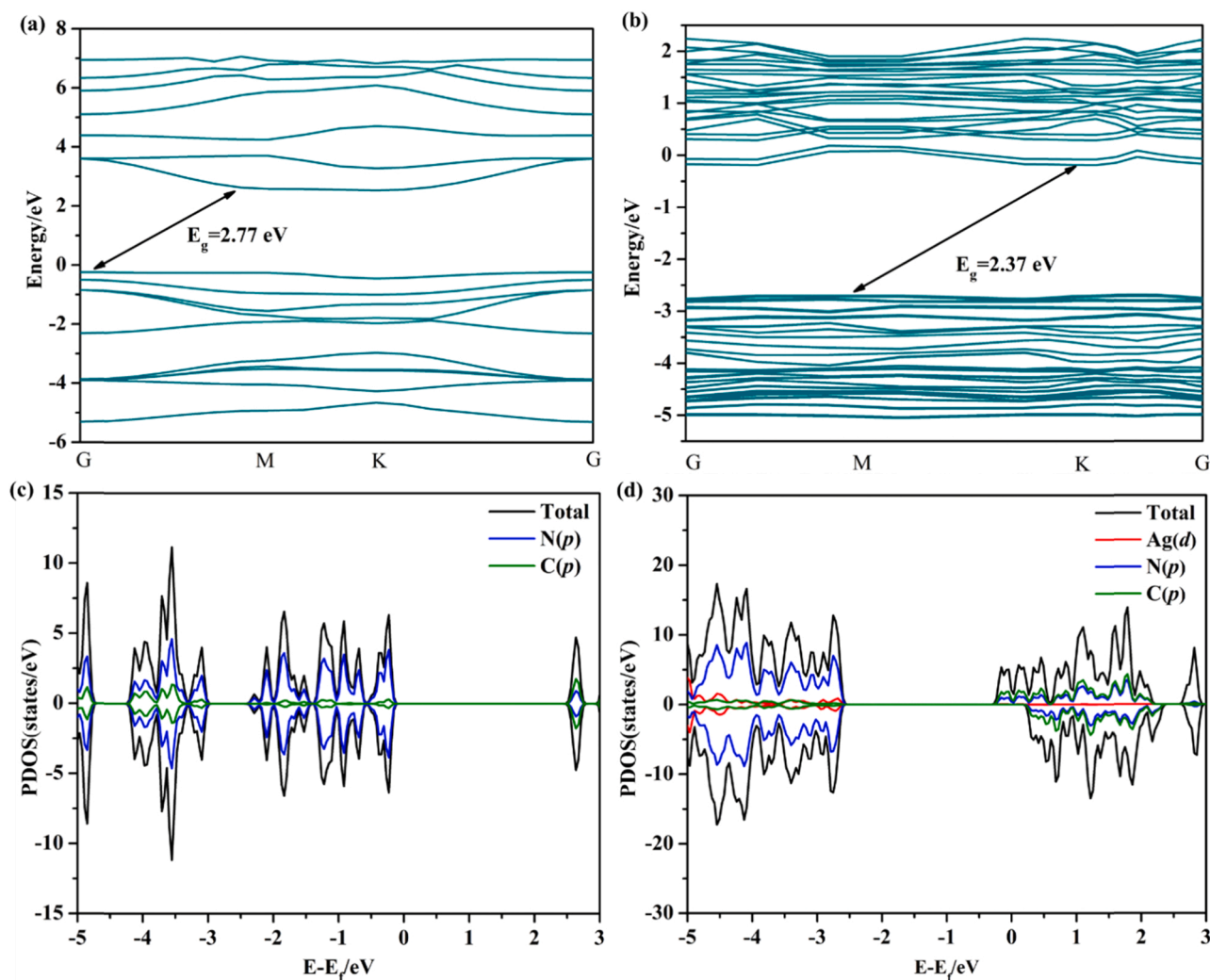


**Fig. 10.** Energy band diagrams of (a) 3DT-CN and (b) SAAg/3DT-CN; PDOS of (c) 3DT-CN and (d) SAAg/3DT-CN under the calculation level of the HSE06 hybrid functional.

theoretical  $E_g$  of SAAg/3DT-CN is reduced by  $\sim 0.4$  eV. SAAg/3DT-CN with a narrower band gap can be excited by lower energy. That is favorable for the utilization of sunlight energy and the generation of electron-hole pairs, resulting in promoting photocatalytic efficiency. From the projected density of state (PDOS), both  $p$  orbital electrons of N ( $N(p)$ ) and C ( $C(p)$ ) contribute to the CBM of 3DT-CN (Fig. 10c), which is consistent with previous reports [74]. It is observed that the  $d$  orbital electrons of silver ( $Ag(d)$ ) contribute to the VBM of SAAg/3DT-CN (Fig. 10d), which promotes single-atom Ag to transfer electrons to electrophilic reactants (such as oxygen), and increases the activity and selectivity of SAAg/3DT-CN [75]. Concurrent,  $Ag(d)$  can be transferred to the  $p$  orbital electrons of carbon and nitrogen, producing more active species on TC. The  $N(p)$  can also be used as an electron transport donor between pyridine nitrogen or graphite nitrogen, improving the efficiency of electron separation. Therefore, it is reasonable to speculate that the extended Vis light absorption range, narrow work function, small band gap and highly active silver atom of SAAg/3DT-CN lead to the boosting catalytic performance in the experiments.

### 3.5. photocatalytic activity tests

To obtain a deeper evaluation of the photodegradation capacity, the degradation of TC experiments was investigated under visible light ( $\lambda > 420$  nm). The photocatalytic degradation efficiency (DE) for TC is

calculated by Eq. (4) [28].

$$DE(\%) = \left(1 - \frac{C_t}{C_0}\right) \times 100\% \quad (4)$$

Where, the concentration of TC is called  $C_t$  after  $t$  minutes and  $C_0$  is the initial concentration of TC. As shown in Fig. 11a, the TC degradation efficiencies of the SAAg-incorporated sample are sharply enhanced in contrast to AgNP/3DT-CN and 3DT-CN. The TC (20 mg/L, 200 mL) is almost completely removed by SAAg/3DT-CN (20 mg) in 75 min, which is much faster than AgNP/3DT-CN. The 3DT-CN and AgNP/3DT-CN only reach 37.54% and 57.09% degradation rates for TC after 75 min. It implies that the synergistic effect of SAAg and hierarchical 3DT-CN plays a nonnegligible role in excellent photocatalytic performance. Meanwhile, the photocatalytic activity of SAAg/3DT-CN for TC treatment is higher than that of most  $g-C_3N_4$ -based photocatalysts compared with previous reported studies (Table 1). It indicates that SAAg/3DT-CN is a favorable photocatalyst for removing organic pollutants.

Moreover, the apparent rate constants ( $k$ ) are calculated by  $\ln(C_0/C_t)$  versus time ( $t$ ) and the corresponding curves are exhibited in Fig. 11b. In addition, the curves show linear relationship, belonging to the pseudo-first-order model [76]. The  $k$  value of the SAAg/3DT-CN is  $0.042 \text{ min}^{-1}$ , which is 8.4 and 3.8 times than that of 3DT-CN ( $0.005 \text{ min}^{-1}$ ) and AgNP/3DT-CN ( $0.011 \text{ min}^{-1}$ ), respectively. The reusability and durability of photocatalysts is an important factor in the

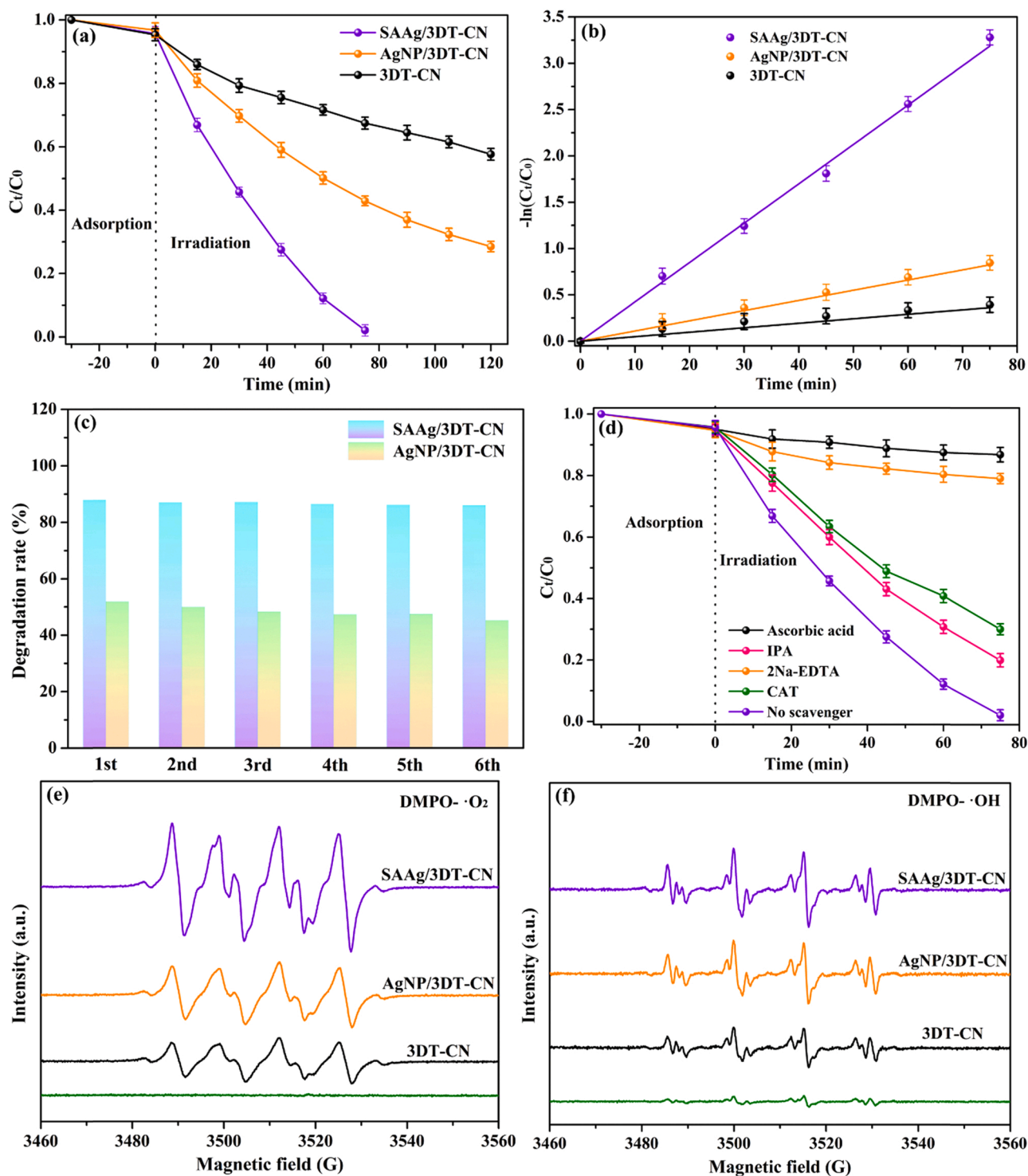


**Fig. 11.** (a) The photocatalytic degradation of TC; (b) pseudo-first-order reaction kinetics; (c) cycle experiments; (d) trapping experiments and (e, f) ESR spectra of as-prepared photocatalysts.

economical removal of pollutants. Six cycles of photocatalytic degradation of TC (Fig. 11c) by SAAg/3DT-CN were carried out. Obviously, the results show that the photocatalytic efficiency is not reduced. Besides, the microstructure of SAAg/3DT-CN (Fig. S6) was verified by TEM after six cycles of the experiment. There is no change in the microstructure of SAAg/3DT-CN and no Ag nanoparticles are produced after the reaction. In addition, the leaching concentration of  $\text{Ag}^+$  at different times in the process of photocatalytic degradation is shown in Fig. S7, ranging from 0.37  $\mu\text{g/L}$  to 1.15  $\mu\text{g/L}$ , which is far less than the national

regulation of  $\text{Ag}^+$  content (0.05 mg/L) in water. The leached amount of  $\text{Ag}^+$  accounted for 0.04% of the total amount in SAAg/3DT-CN. It indicates that SAAg/3DT-CN has excellent reusability. Furthermore, the effect of  $\text{Ag}^+$  on its activity was researched by photocatalytic degradation of TC. The  $\text{AgNO}_3$  solution (1 mmol) was added to the degradation system, and it is found that the degradation efficiency is little effect (Fig. S8). We also studied the effect of  $\text{Ag}^+$  by DFT calculations, as shown in Fig. S9. The system in which  $\text{Ag}^+$  are introduced has slightly fewer electrons (6.16 e) on oxygen than it did before (6.24 e). It means that the

**Table 1**  
Comparison with other g-C<sub>3</sub>N<sub>4</sub>-based photocatalysts for degradation.

Photocatalysts	Pollutant concentration (mg·L <sup>-1</sup> )	Dosage (g·L <sup>-1</sup> )	Light source	Kinetic constant (min <sup>-1</sup> )	Res. (year)
Mo <sub>3</sub> O <sub>4</sub> /g-C <sub>3</sub> N <sub>4</sub>	TC <sup>a</sup> (10)	0.50	500 W XL <sup>b</sup> (λ > 420 nm)	0.010	2018 [77]
CDs <sup>c</sup> /g-C <sub>3</sub> N <sub>4</sub> /MoO <sub>3</sub>	TC (20)	0.60	350 W XL (λ > 420 nm)	0.023	2018 [78]
Co <sub>3</sub> O <sub>4</sub> @CoO/g-C <sub>3</sub> N <sub>4</sub>	TC (10)	0.60	500 W XL (λ > 420 nm)	0.021	2019 [79]
HTCN-C <sup>d</sup>	TC (20)	1.00	300 W XL (λ > 420 nm)	0.029	2019 [80]
BNQDs <sup>e</sup> /UPCN <sup>f</sup>	OTC (10)	1.00	300 W XL (λ > 420 nm)	0.031	2019 [81]
WO <sub>3</sub> /g-C <sub>3</sub> N <sub>4</sub>	TC (20)	1.00	300 W XL (λ > 420 nm)	0.038	2020 [82]
SACo-PCN <sup>g</sup>	OTC (20)	0.30	300 W XL (λ > 420 nm)	0.038	2020 [28]
OCN <sup>h</sup>	OTC (20)	1.00	300 W XL (λ > 420 nm)	0.016	2020 [83]
Bi <sub>2</sub> O <sub>3</sub> QDs <sup>i</sup> /g-C <sub>3</sub> N <sub>4</sub>	TC (10)	0.50	300 W XL (λ > 400 nm)	0.014	2021 [84]
Ag-C <sub>3</sub> N <sub>4</sub> /SnS <sub>2</sub>	TC (15)	0.40	500 W XL (λ > 420 nm)	0.020	2021 [85]
Co/V-g-C <sub>3</sub> N <sub>4</sub>	TC (10)	1.00	250 W XL (λ > 420 nm)	0.011	2021 [76]
AgNP/3DT-CN	TC (20)	1.00	300 W XL (λ > 420 nm)	0.011	this work
SAAg/3DT-CN	TC (20)	1.00	300 W XL (λ > 420 nm)	0.042	this work

<sup>a</sup> TC is tetracycline.

<sup>b</sup> XL is the xenon lamp.

<sup>c</sup> CDs is carbon dots.

<sup>d</sup> HTCN-C is S-doped carbon quantum dots/hollow tubular g-C<sub>3</sub>N<sub>4</sub>.

<sup>e</sup> BNQDs are boron nitride quantum dots.

<sup>f</sup> UPCN is ultrathin porous g-C<sub>3</sub>N<sub>4</sub>.

<sup>g</sup> SACo-PCN is single-atom cobalt on polymeric carbon nitride.

<sup>h</sup> OCN is oxygen-substituted ultrathin porous g-C<sub>3</sub>N<sub>4</sub>.

<sup>i</sup> Bi<sub>2</sub>O<sub>3</sub> QDs are bismuth oxide quantum dots.

introduction of Ag<sup>+</sup> has a negligible effect on the number of electrons. Moreover, the leached amount of Ag<sup>+</sup> is very small in the SAAg/3DT-CN system and then the effect of Ag<sup>+</sup> can be ignored. Therefore, the SAAg/3DT-CN photocatalyst has excellent reusability and durability. To evaluate the mineralization ability of TC in the as-prepared photocatalysts, the total organic carbon (TOC) test results are presented in Fig. S10. The SAAg/3DT-CN displays the highest removal rate (82.41%), which is 2.59 times and 1.75 times higher than those of 3DT-CN (31.84%) and AgNP/3DT-CN (47.18%) in 75 min, respectively. It indicates that SAAg/3DT-CN has excellent mineralization activity and TC molecules can be converted to CO<sub>2</sub> and H<sub>2</sub>O. These results indicate that a synergistic effect existed between SAAg and 3DT-CN to improve the photocatalytic efficiency. Thereby, the photocatalyst, with repeated use and economic value, provides an effective technique for the treatment of refractory antibiotics.

### 3.6. Mechanism investigations

In order to research the reactive oxygen species (ROS) that mainly contribute to the SAAg/3DT-CN reaction process, the capture experiments were carried out by adding trapping agents. Specifically, the ascorbic acid, isopropanol (IPA), ethylenediaminetetraacetic acid disodium (2Na-EDTA) and catalase (CAT) are used to quencher for •O<sub>2</sub><sup>-</sup>, •OH, h<sup>+</sup> and H<sub>2</sub>O<sub>2</sub>, respectively. As depicted in Fig. 11d, when 3DT-CN and SAAg act synergically on TC, different trapping agents have different effects. The addition of IPA leads to slight inhibition on the efficiency of TC treatment (80.04%), indicating that the •OH radicals occupy the minor position in the reaction. The inhibition effect of CAT on the TC degradation efficiency is slightly higher than that of IPA,

indicating that H<sub>2</sub>O<sub>2</sub> generated in situ contributed more to the TC degradation than •OH radicals and H<sub>2</sub>O<sub>2</sub> is responsible for the production of •OH radicals. Surprisingly, the degradation rates are significantly suppressed with the addition of ascorbic acid (13.17%) and 2Na-EDTA (20.94%). Thus, •O<sub>2</sub><sup>-</sup> radicals and h<sup>+</sup> are the predominant active species during the photodegradation of TC by SAAg/3DT-CN. Additionally, the ROS generated also persuasively demonstrate the 5,5-dimethyl-1-pyrroline N-oxide (DMPO) by electron spin-trapping spectroscopy (ESR). No ESR signals are monitored under dark conditions, as shown in Fig. 11e-f. Whereas, the obvious ESR signals with the intensity ratios of 1:1:1:1 and 1:2:2:1, attributing to the DMPO-•O<sub>2</sub><sup>-</sup> and DMPO-•OH adducts, are found under Vis light irradiation. That is, the •O<sub>2</sub><sup>-</sup> and •OH radicals are dominant active species. It is consistent with the results of capture experiments. Furthermore, the •O<sub>2</sub><sup>-</sup> radicals signal peaks of SAAg/3DT-CN are stronger than that of 3DT-CN and AgNP/3DT-CN, indicating that more •O<sub>2</sub><sup>-</sup> radicals can be generated after the introduction of SAAg. Interestingly, the similar trend results are presented in Fig. 11f for •OH radicals' generation. However, the obtained results from trapping experiments demonstrate that •OH radicals have little effect on TC degradation for SAAg/3DT-CN. This phenomenon might be attributed to the further reduction of •O<sub>2</sub><sup>-</sup> radicals via •O<sub>2</sub><sup>-</sup> → H<sub>2</sub>O<sub>2</sub> → •OH. Obviously, •OH radicals have a lower signal than •O<sub>2</sub><sup>-</sup> radicals, implying that •OH radicals do not play a major role. In addition, the ESR intensity of DMPO-•OH after adding CAT is presented in Fig. S11. Obviously, the signal peak intensity of DMPO-•OH is weakened, indicating that •OH radicals are derived from H<sub>2</sub>O<sub>2</sub>. Therefore, •OH radicals are detected in Fig. 11f because •O<sub>2</sub><sup>-</sup> radicals react with electrons to form part of H<sub>2</sub>O<sub>2</sub> and further become part of the •OH radicals.

Moreover, the Mott-Schottky (M-S) technique is applied to measure the position of flat band potentials, achieving the purpose of comprehending the photocatalytic mechanism. The position of flat band potentials are -1.24 V (3DT-CN) and -1.02 V (SAAg/3DT-CN) in Fig. 12a-b. It implies that the conduction band (CB) positions are -1.04 V and -0.82 V for the standard hydrogen electrode. The slopes of 3DT-CN and SAAg/3DT-CN in the M-S curves are positive, indicating that the samples, with electrons as the majority carriers, are typical n-type semiconductors. The E<sub>g</sub> of 3DT-CN (2.50 eV) and SAAg/3DT-CN (2.24 eV) have already been estimated by the Kubelka-Munk theory in Fig. 6b. In addition, the test values of the valence band (VB) spectra are presented in Fig. 12c-d. The actual valence band (VB) positions of 3DT-CN (1.46 V) and SAAg/3DT-CN (1.42 V) are calculated by the formula E<sub>NHE</sub>/V = 4.63 + f - 4.44 (E<sub>NHE</sub>: potential of normal hydrogen electrode; f: the test value of VB spectra). Furthermore, the VB positions are further verified by the formula E<sub>VB</sub> = E<sub>CB</sub> + E<sub>g</sub> and have similar results. Consequently, the band structure diagrams of as-prepared samples are shown in Fig. S12.

Based on the above analysis of the experimental results and electronic structure analysis, the photocatalytic degradation mechanism of TC using SAAg/3DT-CN is proposed in Fig. 13. The excellent photocatalytic efficiency is attributed to the synergistic effect of 3DT-CN and SAAg. Specifically, multi-channel 3DT-CN provides more paths for electrons transport in the reaction process and improves the carriers' separation efficiency. Under visible light irradiation, the SAAg/3DT-CN is activated to generate electrons (e<sup>-</sup>) and holes (h<sup>+</sup>) (Eq. (5)). The conduction band (CB) position is located at -0.82 V vs normal hydrogen electrode (NHE) for SAAg/3DT-CN. That is more negative than the redox potential of O<sub>2</sub>/•O<sub>2</sub><sup>-</sup> (-0.33 V vs NHE). Thereby, the e<sup>-</sup> from CB trap the O<sub>2</sub> to form •O<sub>2</sub><sup>-</sup> radicals (Eq. (6)) degrading the TC into CO<sub>2</sub> and H<sub>2</sub>O. The VB of the SAAg/3DT-CN (1.42 V) cannot oxidize H<sub>2</sub>O directly to produce •OH radicals (E<sup>0</sup>(H<sub>2</sub>O/•OH) = 2.38 V). Furthermore, the CB level of SAAg/3DT-CN (-0.82 V) is more negative than the redox potential of H<sub>2</sub>O<sub>2</sub>/•OH (+0.69 V). Therefore, the detected •OH radicals and H<sub>2</sub>O<sub>2</sub> are to be generated by •O<sub>2</sub><sup>-</sup> radicals reacting with e<sup>-</sup> and H<sup>+</sup> to form •OH radicals and have a subtle effect on TC (Eq. (7) and Eq. (8)). To prove whether H<sub>2</sub>O<sub>2</sub> is produced during degradation, the

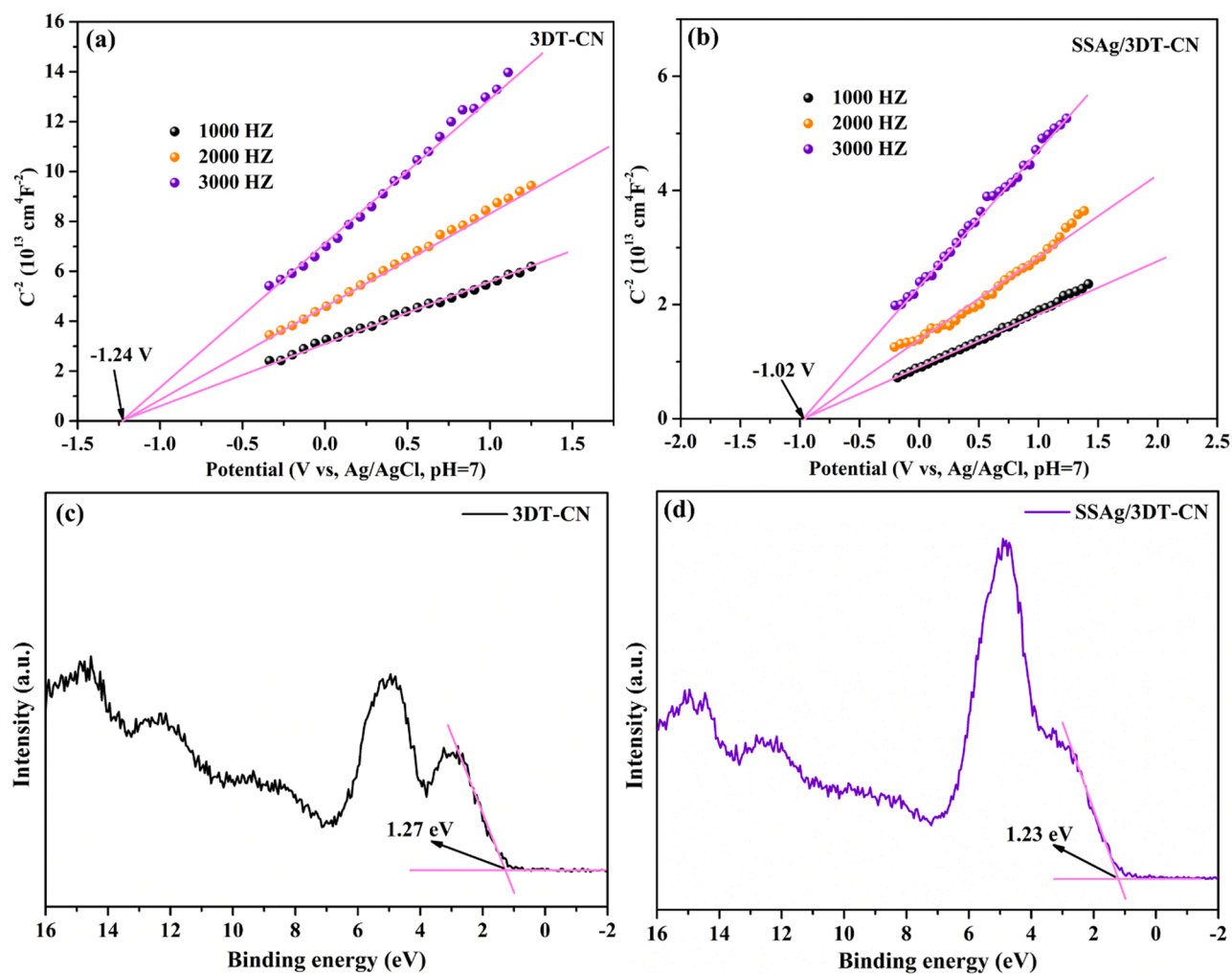


Fig. 12. (a, b) Mott-Schottky plots and (c, d) VB XPS spectra of 3DT-CN and SAAg/3DT-CN.

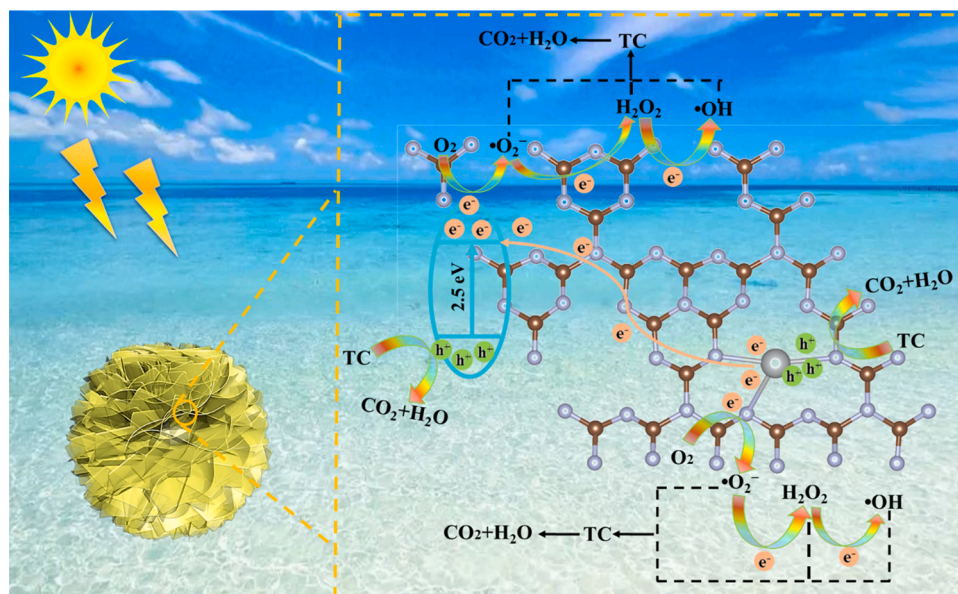
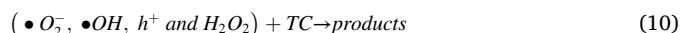
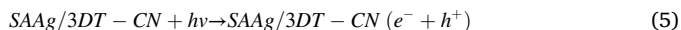


Fig. 13. The proposed photocatalytic degradation mechanism of TC in SAAg/3DT-CN.

concentration of  $\text{H}_2\text{O}_2$  was measured by potassium iodide spectrophotometry, which indicated that the concentration is less than  $18.4 \mu\text{mol/L}$  (Fig. S13). Moreover, the  $\text{h}^+$  can react with  $\text{H}_2\text{O}$  to provide  $\text{O}_2$  for the redox reaction (Eq. (9)), producing more active species. Additionally,  $\text{h}^+$  can directly act on TC degradation into small molecules (Eq. (10)). DFT calculations have shown that the introduction of SAAg makes it easier for the photocatalyst to bond with  $\text{O}_2$ , so the electrons around SAAg will continue to be picked up by  $\text{O}_2$ , creating more  $\bullet\text{O}_2^-$  radicals to act on TC. Simultaneously, the electrons of SAAg are also transferred to 3DT-CN, facilitating carriers' separation efficiency. In addition to the narrower band gap and the corresponding enhancement of the light absorption of SAAg/3DT-CN, the previously discussed "catfish effect" also benefits in boosting the photocatalytic performance. In summary, the synergistic effect of SAAg and 3DT-CN not only regulates the electronic structure but also furnishes multiple carriers transfer channels.



#### 4. Conclusions

In summary, SAAg embedded in a fractional 3DT-CN unit photocatalyst was successfully fabricated by an efficient one-step reduction method. In particular, based on comprehensive characterizations and analysis using AC-HAADF-STEM, XANES and EXAFS, the successful introduction of single-atom Ag in 3DT-CN with a quite tiny level has been proven. DFT calculations, UV-vis DRS, PL, TR-PL, and electrochemical tests have demonstrated that SAAg/3DT-CN exhibits some properties, including excellent interface electronic regulation, multiple electron transport channels and the promotion of charge separation and transfer efficiency. Typically, the single-atom Ag embedded in the structure of tri-s-triazine units results in a perturbation in the conjugated aromatic system, linking the "catfish effect", subsequently leading to the improvement of electron migration or transmission ability. Visible light capture and absorptivity are also enhanced simultaneously, which also benefits in the improvement of the photocatalytic performance. The TC (20 mg/L, 200 mL) is almost completely removed by SAAg/3DT-CN (20 mg) in 75 min, which is much faster than AgNP/3DT-CN. The  $k$  value of SAAg/3DT-CN is  $0.042 \text{ min}^{-1}$ , which is 8.4 and 3.8 times that of 3DT-CN and AgNP/3DT-CN, respectively. ESR experiments and capture experiments show that  $\bullet\text{O}_2^-$  and  $\text{h}^+$  are the main active species in the mechanism of the synergistic action of SAAg and 3DT-CN on TC. In addition, the binding energy of SAAg/3DT-CN for  $\text{O}_2$  is  $-0.63 \text{ eV}$ , which is greater than that of 3DT-CN ( $-0.42 \text{ eV}$ ). It indicates that SAAg/3DT-CN can absorb more  $\text{O}_2$ , resulting in more active species.

#### CRediT authorship contribution statement

**Linlin Sun:** Investigation, Data curation, Formal analysis, Writing – original draft. **Yibing Feng:** Investigation, Visualization. **Kai Ma:** Conceptualization, Visualization. **Xiaohan Jiang:** Investigation, Visualization. **Zhengyang Gao:** Project administration, Software. **Jigang Wang:** Writing–review & editing, Project administration, Funding acquisition. **Nan Jiang:** Methodology, Writing – review & editing. **Xiaoshuo Liu:** Conceptualization, Formal analysis.

#### Declaration of Competing Interest

The authors declare that they have no known competing financial interests or personal relationships that could have appeared to influence the work reported in this paper.

#### Acknowledgement

We gratefully acknowledge the financial support of the National Natural Science Foundation of China (21776117), Six talent peaks project in Jiangsu Province (XCL-014), National Key Research and Development Program of China (2016YFA0202401), the Beijing Natural Science Foundation (2182066), the Key Project of Tibet Natural Science Foundation (XZ2017ZRG-66(Z)) and the Natural Science Foundation of Hebei Province of China (B2018502067).

#### Appendix A. Supporting information

Supplementary data associated with this article can be found in the online version at doi:10.1016/j.apcatb.2022.121106.

#### References

- [1] Q. Zhang, L. Jiang, J. Wang, Y. Zhu, Y. Pu, W. Dai, Photocatalytic degradation of tetracycline antibiotics using three-dimensional network structure perylene diimide supramolecular organic photocatalyst under visible-light irradiation, *Appl. Catal. B: Environ.* 277 (2020), 119122, <https://doi.org/10.1016/j.apcatb.2020.119122>.
- [2] H. Yin, G. Li, X. Chen, W. Wang, P.K. Wong, H. Zhao, T. An, Accelerated evolution of bacterial antibiotic resistance through early emerged stress responses driven by photocatalytic oxidation, *Appl. Catal. B: Environ.* 269 (2020), 118829, <https://doi.org/10.1016/j.apcatb.2020.118829>.
- [3] Y. Yang, W. Song, H. Lin, W. Wang, L. Du, W. Xing, Antibiotics and antibiotic resistance genes in global lakes: a review and meta-analysis, *Environ. Int.* 116 (2018) 60–73, <https://doi.org/10.1016/j.envint.2018.04.011>.
- [4] H. Shen, M. Wang, X. Zhang, D. Li, G. Liu, W. Shi, 2D/2D/3D architecture Z-scheme system for simultaneous  $\text{H}_2$  generation and antibiotic degradation, *Fuel* 280 (2020), 118618, <https://doi.org/10.1016/j.fuel.2020.118618>.
- [5] S. Tian, C. Zhang, D. Huang, R. Wang, G. Zeng, M. Yan, W. Xiong, C. Zhou, M. Cheng, W. Xue, Y. Yang, W. Wang, Recent progress in sustainable technologies for adsorptive and reactive removal of sulfonamides, *Chem. Eng. J.* 389 (2020), 123423, <https://doi.org/10.1016/j.cej.2019.123423>.
- [6] Y. Wang, J. He, P. Wu, D. Luo, R. Yan, H. Zhang, W. Jiang, Simultaneous removal of tetracycline and Cu(II) in hybrid wastewater through formic-acid-assisted  $\text{TiO}_2$  photocatalysis, *Ind. Eng. Chem. Res.* 59 (2020) 15098–15108, <https://doi.org/10.1021/acs.iecr.0c02443>.
- [7] X. Liu, Y. Yang, H. Li, Z. Yang, Y. Fang, Visible light degradation of tetracycline using oxygen-rich titanium dioxide nanosheets decorated by carbon quantum dots, *Chem. Eng. J.* 408 (2021), 127259, <https://doi.org/10.1016/j.cej.2020.127259>.
- [8] Z. Lu, G. Zhou, M. Song, D. Wang, P. Huo, W. Fan, H. Dong, H. Tang, F. Yan, G. Xing, Magnetic functional heterojunction reactors with 3D specific recognition for selective photocatalysis and synergistic photodegradation in binary antibiotic solutions, *J. Mater. Chem. A* 7 (2019) 13986–14000, <https://doi.org/10.1039/C9TA01863H>.
- [9] M.A. Wahab, C.M. Hasan, Z.A. Allothman, M.S.A. Hossain, In-situ incorporation of highly dispersed silver nanoparticles in nanoporous carbon nitride for the enhancement of antibacterial activities, *J. Hazard. Mater.* 408 (2021), 124919, <https://doi.org/10.1016/j.jhazmat.2020.124919>.
- [10] X. Li, N. Wang, X. Liang, G. Xu, X. Li, J. Jiao, J. Lou, Y. Hashad, Safety and efficacy of dexamethasone intravitreal implant for treatment of macular edema secondary to retinal vein occlusion in chinese patients: randomized, sham-controlled, multicenter study, *Graef. Arch. Clin. Exp.* 256 (2018) 59–69, <https://doi.org/10.1007/s00417-017-3831-6>.
- [11] Q. Shen, L. Wei, R. Bibi, K. Wang, D. Hao, J. Zhou, N. Li, Boosting photocatalytic degradation of tetracycline under visible light over hierarchical carbon nitride microrods with carbon vacancies, *J. Hazard. Mater.* 413 (2021), 125376, <https://doi.org/10.1016/j.jhazmat.2021.125376>.
- [12] Y. Hong, C. Li, B. Yin, D. Li, Z. Zhang, B. Mao, W. Fan, W. Gu, W. Shi, Promoting visible-light-induced photocatalytic degradation of tetracycline by an efficient and stable  $\beta\text{-Bi}_2\text{O}_3/\text{g-C}_3\text{N}_4$  core/shell nanocomposite, *Chem. Eng. J.* 338 (2018) 137–146, <https://doi.org/10.1016/j.cej.2019.123500>.
- [13] G. Li, B. Wang, J. Zhang, R. Wang, H. Liu, Er-doped g-C<sub>3</sub>N<sub>4</sub> for photodegradation of tetracycline and tylosin: high photocatalytic activity and low leaching toxicity, *Chem. Eng. J.* 391 (2020), 123500, <https://doi.org/10.1016/j.cej.2019.123500>.
- [14] X. Li, W. Wang, F. Dong, Z. Zhang, L. Han, X. Luo, J. Huang, Z. Feng, Z. Chen, G. Jia, T. Zhang, Recent advances in noncontact external-field-assisted photocatalysis: from fundamentals to applications, *ACS Catal.* 11 (2021) 4739–4769, <https://doi.org/10.1021/acscatal.0c05354>.

- [15] Y. Bao, W.J. Lee, J.Z.Y. Seow, H. Hara, Y.N. Liang, H. Feng, J.Z. Xu, T. Lim, X. Hu, One-Step block copolymer templated synthesis of bismuth oxybromide for bisphenol A degradation: an extended study from photocatalysis to chemical oxidation, *ACS EST. Water* 1 (2021) 837–846, <https://doi.org/10.1021/acsestwater.0c00190>.
- [16] Z. Du, L. Feng, Z. Guo, T. Yan, Q. Hu, J. Lin, Y. Huang, C. Tang, Y. Fang, Ultrathin h-BN/Bi<sub>2</sub>MoO<sub>6</sub> heterojunction with synergetic effect for visible-light photocatalytic tetracycline degradation, *J. Colloid Interf. Sci.* 589 (2021) 545–555, <https://doi.org/10.1016/j.jcis.2021.01.027>.
- [17] Y. Li, R. Jin, Y. Xing, J. Li, S. Song, X. Liu, M. Li, R. Jin, Macroscopic foam-like holey ultrathin g-C<sub>3</sub>N<sub>4</sub> nanosheets for drastic improvement of visible-light photocatalytic activity, *Adv. Energy Mater.* 6 (2016), 1601273, <https://doi.org/10.1002/aenm.201601273>.
- [18] S. Cao, J. Low, J. Yu, M. Jaroniec, Polymeric photocatalysts based on graphitic carbon nitride, *Adv. Mater.* 27 (2015) 2150–2176, <https://doi.org/10.1002/adma.201500033>.
- [19] Q. Han, B. Wang, J. Gao, Z. Cheng, Y. Zhao, Z. Zhang, L. Qu, Atomically thin mesoporous nanomesh of graphitic C<sub>3</sub>N<sub>4</sub> for high-efficiency photocatalytic hydrogen evolution, *ACS Nano* 10 (2016) 2745–2751, <https://doi.org/10.1021/acsnano.5b07831>.
- [20] Y. Zhong, C. Peng, Z. He, D. Chen, H. Jia, J. Zhang, H. Ding, X. Wu, Interface engineering of heterojunction photocatalysts based on 1D nanomaterials, *Catal. Sci. Technol.* 11 (2021) 27–42, <https://doi.org/10.1039/D0CY01847C>.
- [21] M. Moradi, F. Hasanvandian, A.A. Isari, F. Hayati, B. Kakavandi, S.R. Setayesh, CuO and ZnO co-anchored on g-C<sub>3</sub>N<sub>4</sub> nanosheets as an affordable double Z-scheme nanocomposite for photocatalytic decontamination of amoxicillin, *Appl. Catal. B: Environ.* 285 (2021), 119838, <https://doi.org/10.1016/j.apcatb.2020.119838>.
- [22] T. Song, L. Hou, B. Long, A. Ali, G. Deng, Constructing ultralong hollow chain-ball-like carbon nitride implanted with oxygen for superior visible-light photocatalytic hydrogen production, *J. Alloy. Compd.* 857 (2021), 157609, <https://doi.org/10.1016/j.jallcom.2020.157609>.
- [23] X. Dang, R. Yang, Z. Wang, S. Wu, H. Zhao, Efficient visible-light activation of molecular oxygen to produce hydrogen peroxide using P doped g-C<sub>3</sub>N<sub>4</sub> hollow spheres, *J. Mater. Chem. A* 8 (2020) 22720–22727, <https://doi.org/10.1039/D0TA07794A>.
- [24] X. Li, T. Wan, J. Qiu, H. Wei, F. Qin, Y. Wang, Y. Liao, Z. Huang, X. Tan, In-situ photocalorimetry-fluorescence spectroscopy studies of RhB photocatalysis over Z-scheme g-C<sub>3</sub>N<sub>4</sub>@Ag@Ag<sub>3</sub>PO<sub>4</sub> nanocomposites: a pseudo-zero-order rather than a first-order process, *Appl. Catal. B: Environ.* 217 (2017) 591–602, <https://doi.org/10.1016/j.apcatb.2017.05.086>.
- [25] Z. Dai, Y. Zhen, Y. Sun, L. Li, D. Ding, ZnFe<sub>2</sub>O<sub>4</sub>/g-C<sub>3</sub>N<sub>4</sub> S-scheme photocatalyst with enhanced adsorption and photocatalytic activity for uranium(VI) removal, *Chem. Eng. J.* 415 (2021), 129002, <https://doi.org/10.1016/j.cej.2021.129002>.
- [26] C. Yang, Z. Cheng, G. Divitini, C. Qian, B. Hou, Y. Liao, A Ni or Co single atom anchored conjugated microporous polymer for high-performance photocatalytic hydrogen evolution, *J. Mater. Chem. A* 9 (2021) 19894–19900, <https://doi.org/10.1039/D1TA02547C>.
- [27] Y. Yang, F. Li, J. Chen, J. Fan, Q. Xiang, Single Au atoms anchored on amino-group-enriched graphitic carbon nitride for photocatalytic CO<sub>2</sub> reduction, *ChemSusChem* 13 (2020) 1979–1985, <https://doi.org/10.1002/cssc.202000375>.
- [28] Y. Yang, G. Zeng, D. Huang, C. Zhang, D. He, C. Zhou, W. Wang, W. Xiong, B. Song, H. Yi, S. Ye, X. Ren, In situ grown single-atom cobalt on polymeric carbon nitride with bidentate ligand for efficient photocatalytic degradation of refractory antibiotics, *Small* 16 (2020), 2001634, <https://doi.org/10.1002/sml.202001634>.
- [29] X. Jiang, L. Zhang, H. Liu, D. Wu, F. Wu, L. Tian, L. Liu, J. Zou, S. Luo, B. Chen, Silver single atom in carbon nitride catalyst for highly efficient photocatalytic hydrogen evolution, *Angew. Chem. Int. Ed.* 59 (2020) 23112–23116, <https://doi.org/10.1002/anie.202011495>.
- [30] Z. Zeng, Y. Su, X. Quan, W. Choi, G. Zhang, N. Liu, B. Kim, S. Chen, H. Yu, S. Zhang, Single-atom platinum confined by the interlayer nanospace of carbon nitride for efficient photocatalytic hydrogen evolution, *Nano Energy* 69 (2020), 104409, <https://doi.org/10.1016/j.nanoen.2019.104409>.
- [31] Z. Zhou, Z. Shen, C. Song, M. Li, H. Li, S. Zhan, Boosting the activation of molecular oxygen and the degradation of tetracycline over high loading Ag single atomic catalyst, *Water Res* 201 (2021), 117314, <https://doi.org/10.1016/j.watres.2021.117314>.
- [32] W. Liu, W. Hu, L. Yang, J. Liu, Single cobalt atom anchored on carbon nitride with well-defined active sites for photo-enzyme catalysis, *Nano Energy* 73 (2020), 104750, <https://doi.org/10.1016/j.nanoen.2020.104750>.
- [33] Z. Chen, S. Pronkin, T.P. Fellerling, K. Kailasam, G. Vile, D. Albani, F. Krumeich, R. Leary, J. Barnard, J.M. Thomas, J. Perez-Ramirez, M. Antonietti, D. Dontsova, Merging single-atom-dispersed silver and carbon nitride to a joint electronic system via copolymerization with silver tricyanomethanide, *ACS Nano* 10 (2016) 3166–3175, <https://doi.org/10.1021/acsnano.5b04210>.
- [34] X. Zhou, B. Shen, J. Zhai, N. Hedin, Reactive oxygenated species generated on iodide-doped BiVO<sub>4</sub>/BaTiO<sub>3</sub> heterostructures with Ag/Cu nanoparticles by coupled piezophototronic effect and plasmonic excitation, *Adv. Funct. Mater.* 31 (2021), 2009594, <https://doi.org/10.1002/adfm.202009594>.
- [35] Y. Oh, J.O. Hwang, E.S. Lee, M. Yoon, V.D. Le, Y.H. Kim, D.H. Kim, S.O. Kim, Divalent Fe atom coordination in two-dimensional microporous graphitic carbon nitride, *ACS Appl. Mater. Interf.* 8 (2016) 25438–25443, <https://doi.org/10.1021/acsami.6b07287>.
- [36] J. Huang, B. Wang, Z. Hao, Z. Zhou, Y. Qu, Boosting charge separation and broadening NIR light response over defected WO<sub>3</sub> quantum dots coupled g-C<sub>3</sub>N<sub>4</sub> nanosheets for photocatalytic degrading antibiotics, *Chem. Eng. J.* 416 (2021), 129109, <https://doi.org/10.1016/j.cej.2021.129109>.
- [37] Z. Liu, J. Huang, B. Shao, H. Zhong, Q. Liang, Q. He, T. Wu, Y. Pan, Z. Peng, X. Yuan, Y. Liu, C. Zhao, In-situ construction of 2D/1D Bi<sub>2</sub>O<sub>2</sub>CO<sub>3</sub> nanoflake/S-doped g-C<sub>3</sub>N<sub>4</sub> hollow tube hierarchical heterostructure with enhanced visible-light photocatalytic activity, *Chem. Eng. J.* 426 (2021), 130767, <https://doi.org/10.1016/j.cej.2021.130767>.
- [38] X. Tian, Y. Sun, J. He, X. Wang, J. Zhao, S. Qiao, F. Li, Surface P atom grafting of g-C<sub>3</sub>N<sub>4</sub> for improved local spatial charge separation and enhanced photocatalytic H<sub>2</sub> production, *J. Mater. Chem. A* 7 (2019) 7628–7635, <https://doi.org/10.1039/C9TA00129H>.
- [39] H. Zhao, G. Li, F. Tian, Q. Jia, Y. Liu, R. Chen, g-C<sub>3</sub>N<sub>4</sub> surface-decorated Bi<sub>2</sub>O<sub>2</sub>CO<sub>3</sub> for improved photocatalytic performance: theoretical calculation and photodegradation of antibiotics in actual water matrix, *Chem. Eng. J.* 366 (2019) 468–479, <https://doi.org/10.1016/j.cej.2019.02.088>.
- [40] S. Yu, J. Li, Y. Zhang, M. Li, F. Dong, T. Zhang, H. Huang, Local spatial charge separation and proton activation induced by surface hydroxylation promoting photocatalytic hydrogen evolution of polymeric carbon nitride, *Nano Energy* 50 (2018) 383–392, <https://doi.org/10.1016/j.nanoen.2018.05.053>.
- [41] S. Cao, H. Chen, F. Jiang, X. Wang, Nitrogen photofixation by ultrathin amine-functionalized graphitic carbon nitride nanosheets as a gaseous product from thermal polymerization of urea, *Appl. Catal. B: Environ.* 224 (2018) 222–229, <https://doi.org/10.1016/j.apcatb.2017.10.028>.
- [42] S. Lv, Y.H. Ng, R. Zhu, S. Li, C. Wu, Y. Liu, Y. Zhang, L. Jing, J. Deng, H. Dai, Phosphorus vapor assisted preparation of P-doped ultrathin hollow g-C<sub>3</sub>N<sub>4</sub> sphere for efficient solar-to-hydrogen conversion, *Appl. Catal. B: Environ.* 297 (2021), 120438, <https://doi.org/10.1016/j.apcatb.2021.120438>.
- [43] A. Kula, P. Saravanan, D. Bahnemann, C. Wang, Novel Ag decorated, BiOCl surface doped AgVO<sub>3</sub> nanobelt ternary composite with Z-scheme homojunction-heterojunction interface for high prolific photo switching, quantum efficiency and hole mediated photocatalysis, *Appl. Catal. B: Environ.* 293 (2021), 120224, <https://doi.org/10.1016/j.apcatb.2021.120224>.
- [44] J. Chen, X. Xiao, Y. Wang, Z. Ye, Ag nanoparticles decorated WO<sub>3</sub>/g-C<sub>3</sub>N<sub>4</sub> 2D/2D heterostructure with enhanced photocatalytic activity for organic pollutants degradation, *Appl. Surf. Sci.* 467–468 (2019) 1000–1010, <https://doi.org/10.1016/j.apsusc.2018.10.236>.
- [45] Y. Li, B. Li, D. Zhang, L. Cheng, Q. Xiang, Crystalline carbon nitride supported copper single atoms for photocatalytic CO<sub>2</sub> reduction with nearly 100% CO selectivity, *ACS Nano* 14 (2020) 10552–10561, <https://doi.org/10.1021/acsnano.0c04544>.
- [46] J. Zhu, X. Zhu, F. Cheng, P. Li, F. Wang, Y. Xiao, W. Xiong, Preparing copper doped carbon nitride from melamine templated crystalline copper chloride for Fenton-like catalysis, *Appl. Catal. B: Environ.* 256 (2019), 117830, <https://doi.org/10.1016/j.apcatb.2019.117830>.
- [47] X.-H. Li, X. Wang, M. Antonietti, Solvent-free and metal-free oxidation of toluene using O<sub>2</sub> and g-C<sub>3</sub>N<sub>4</sub> with nanopores: nanostructure boosts the catalytic selectivity, *ACS Catal.* 2 (2012) 2082–2086, <https://doi.org/10.1021/cs300413x>.
- [48] X. Zhang, J. Yan, F. Zheng, J. Zhao, L.Y.S. Lee, Designing charge transfer route at the interface between WP nanoparticle and g-C<sub>3</sub>N<sub>4</sub> for highly enhanced photocatalytic CO<sub>2</sub> reduction reaction, *Appl. Catal. B: Environ.* 286 (2021), 119879, <https://doi.org/10.1016/j.apcatb.2021.119879>.
- [49] R. Wang, Y. Lin, H. Chen, W. Lin, Energy harvesting from g-C<sub>3</sub>N<sub>4</sub> piezoelectric nanogenerators, *Nano Energy* 83 (2021), 105743, <https://doi.org/10.1016/j.nanoen.2021.105743>.
- [50] Z. Zhao, W. Zhang, W. Liu, Y. Li, J. Ye, J. Liang, M. Tong, Single-atom silver induced amorphization of hollow tubular g-C<sub>3</sub>N<sub>4</sub> for enhanced visible light-driven photocatalytic degradation of naproxen, *Sci. Total Environ.* 742 (2020), 140642, <https://doi.org/10.1016/j.scitotenv.2020.140642>.
- [51] F. Wang, Y. Wang, Y. Feng, Y. Zeng, Z. Xie, Q. Zhang, Y. Su, P. Chen, Y. Liu, K. Yao, W. Lv, G. Liu, Novel ternary photocatalyst of single atom-dispersed silver and carbon quantum dots co-loaded with ultrathin g-C<sub>3</sub>N<sub>4</sub> for broad spectrum photocatalytic degradation of naproxen, *Appl. Catal. B: Environ.* 221 (2018) 510–520, <https://doi.org/10.1016/j.apcatb.2017.09.055>.
- [52] J. Ran, T.Y. Ma, G. Gao, X.-W. Du, S.Z. Qiao, Porous P-doped graphitic carbon nitride nanosheets for synergistically enhanced visible-light photocatalytic H<sub>2</sub> production, *Energ. Environ. Sci.* 8 (2015) 3708–3717, <https://doi.org/10.1039/C5EE02650D>.
- [53] P. Sharma, S. Kumar, O. Tomanec, M. Petr, J. Zhu Chen, J.T. Miller, R.S. Varma, M. B. Gawande, R. Zboril, Carbon nitride-based ruthenium single atom photocatalyst for CO<sub>2</sub> reduction to methanol, *Small* 17 (2021), 2006478, <https://doi.org/10.1002/sml.202006478>.
- [54] Z. Wei, F. Yue, Z. Jin, Z. Fengxia, S. Zhenhuan, D. Benlin, D.Y.C. Leung, Z. Lili, X. Jiming, Novel Ag/p-AgBr/n-BiVO<sub>4</sub> plasmonic heterojunction photocatalyst: study on the excellent photocatalytic performance and photocatalytic mechanism, *ACS Appl. Energ. Mater.* 2 (2018) 694–704, <https://doi.org/10.1021/acsaem.8b01737>.
- [55] Y. Chen, C. Shen, J. Wang, G. Xiao, G. Luo, Green synthesis of Ag–TiO<sub>2</sub> supported on porous glass with enhanced photocatalytic performance for oxidative desulfurization and removal of dyes under visible light, *ACS Sustain. Chem. Eng.* 6 (2018) 13276–13286, <https://doi.org/10.1021/acssuschemeng.8b02860>.
- [56] L. Sun, S. Yin, D. Shen, Y. Zhou, J. Li, X. Li, H. Wang, P. Huo, Y. Yan, Fabricating acid-sensitive controlled PAA@Ag/AgCl/CN photocatalyst with reversible photocatalytic activity transformation, *J. Colloid Interf. Sci.* 580 (2020) 753–767, <https://doi.org/10.1016/j.jcis.2020.07.002>.
- [57] K. Bai, Z. Cui, E. Li, Y. Ding, J. Zheng, Y. Zheng, C. Liu, Adsorption of alkali metals on graphitic carbon nitride: a first-principles study, *Mod. Phys. Lett. B* 34 (2020), 2050361, <https://doi.org/10.1142/S0217984920503613>.

- [58] Y. Chen, F. Su, H. Xie, R. Wang, C. Ding, J. Huang, Y. Xu, L. Ye, One-step construction of S-scheme heterojunctions of N-doped MoS<sub>2</sub> and S-doped g-C<sub>3</sub>N<sub>4</sub> for enhanced photocatalytic hydrogen evolution, *Chem. Eng. J.* 404 (2021), 126498, <https://doi.org/10.1016/j.cej.2020.126498>.
- [59] S. Cao, H. Li, T. Tong, H. Chen, A. Yu, J. Yu, H.M. Chen, Single-atom engineering of directional charge transfer channels and active sites for photocatalytic hydrogen evolution, *Adv. Funct. Mater.* 28 (2018), 1802169, <https://doi.org/10.1002/adfm.201802169>.
- [60] Y. Yu, W. Yan, X. Wang, P. Li, W. Gao, H. Zou, S. Wu, K. Ding, Surface engineering for extremely enhanced charge separation and photocatalytic hydrogen evolution on g-C<sub>3</sub>N<sub>4</sub>, *Adv. Mater.* 30 (2018), 1705060, <https://doi.org/10.1002/adma.201705060>.
- [61] Z. Chen, T. Fan, X. Yu, Q. Wu, Q. Zhu, L. Zhang, J. Li, W. Fang, X. Yi, Gradual carbon doping of graphitic carbon nitride towards metal-free visible light photocatalytic hydrogen evolution, *J. Mater. Chem. A* 6 (2018) 15310–15319, <https://doi.org/10.1039/C8TA03303J>.
- [62] M.Z. Rahman, P.C. Tapping, T.W. Kee, R. Smernik, N. Spooner, J. Moffatt, Y. Tang, K. Davey, S.Z. Qiao, A benchmark quantum yield for water photoreduction on amorphous carbon nitride, *Adv. Funct. Mater.* 27 (2017), 1702384, <https://doi.org/10.1002/adfm.201702384>.
- [63] Y. Yang, C. Zhang, D. Huang, G. Zeng, J. Huang, C. Lai, C. Zhou, W. Wang, H. Guo, W. Xue, R. Deng, M. Cheng, W. Xiong, Boron nitride quantum dots decorated ultrathin porous g-C<sub>3</sub>N<sub>4</sub>: intensified exciton dissociation and charge transfer for promoting visible-light-driven molecular oxygen activation, *Appl. Catal. B: Environ.* 245 (2019) 87–99, <https://doi.org/10.1016/j.apcatb.2018.12.049>.
- [64] H. Zhang, J. He, C. Zhai, M. Zhu, 2D Bi<sub>2</sub>WO<sub>6</sub>/MoS<sub>2</sub> as a new photo-activated carrier for boosting electrocatalytic methanol oxidation with visible light illumination, *Chin. Chem. Lett.* 30 (2019) 2338–2342, <https://doi.org/10.1016/j.cclet.2019.07.021>.
- [65] H. Zhang, J. Wu, J. Han, L. Wang, W. Zhang, H. Dong, C. Li, Y. Wang, Photocatalyst/enzyme heterojunction fabricated for high-efficiency photoenzyme synergic catalytic degrading bisphenol A in water, *Chem. Eng. J.* 385 (2020), 123764, <https://doi.org/10.1016/j.cej.2019.123764>.
- [66] X. Lian, W. Xue, S. Dong, E. Liu, H. Li, K. Xu, Construction of S-scheme Bi<sub>2</sub>WO<sub>6</sub>/g-C<sub>3</sub>N<sub>4</sub> heterostructure nanosheets with enhanced visible-light photocatalytic degradation for ammonium dinitramide, *J. Hazard. Mater.* 412 (2021), 125217, <https://doi.org/10.1016/j.jhazmat.2021.125217>.
- [67] J. Li, Y. Ma, Z. Ye, M. Zhou, H. Wang, C. Ma, D. Wang, P. Huo, Y. Yan, Fast electron transfer and enhanced visible light photocatalytic activity using multi-dimensional components of carbon quantum dots@3D daisy-like In<sub>2</sub>S<sub>3</sub>/single-wall carbon nanotubes, *Appl. Catal. B: Environ.* 204 (2017) 224–238, <https://doi.org/10.1016/j.apcatb.2016.11.021>.
- [68] M. Karpuraranjith, Y. Chen, S. Rajaboopathi, M. Ramadoss, K. Srinivas, D. Yang, B. Wang, Three-dimensional porous MoS<sub>2</sub> nanobox embedded g-C<sub>3</sub>N<sub>4</sub>@TiO<sub>2</sub> architecture for highly efficient photocatalytic degradation of organic pollutant, *J. Colloid Interf. Sci.* 605 (2021) 613–623, <https://doi.org/10.1016/j.jcis.2021.07.133>.
- [69] L. Sun, Y. Zhou, X. Li, J. Li, D. Shen, S. Yin, H. Wang, P. Huo, Y. Yan, Thermoresponsive functionalized PNIPAM@Ag/Ag<sub>3</sub>PO<sub>4</sub>/CN-heterostructure photocatalyst with switchable photocatalytic activity, *Chinese, J. Catal.* 41 (2020) 1573–1588, [https://doi.org/10.1016/S1872-2067\(20\)63554-9](https://doi.org/10.1016/S1872-2067(20)63554-9).
- [70] S. Emamian, T. Lu, H. Kruse, H. Emamian, Exploring nature and predicting strength of hydrogen bonds: a correlation analysis between atoms-in-molecules descriptors, binding energies, and energy components of symmetry-adapted perturbation theory, *J. Comput. Chem.* 40 (2019) 2868–2881, <https://doi.org/10.1002/jcc.26068>.
- [71] W. Yang, J. Ren, J. Li, H. Zhang, K. Ma, Q. Wang, Z. Gao, C. Wu, I.D. Gates, A novel Fe-Co double-atom catalyst with high low-temperature activity and strong water-resistant for O<sub>3</sub> decomposition: a theoretical exploration, *J. Hazard. Mater.* 421 (2021), 126639, <https://doi.org/10.1016/j.jhazmat.2021.126639>.
- [72] M. Lei, Y. Zhang, M. Wang, W. Yang, Z. Gao, Density functional theory investigation of As<sub>4</sub>, As<sub>2</sub> and AsH<sub>3</sub> adsorption on Ti-doped graphene, *Chem. Eng. J.* 421 (2021), 129747, <https://doi.org/10.1016/j.cej.2021.129747>.
- [73] Z. Ma, Z. Cui, Y. Lv, R. Sa, K. Wu, Q. Li, Three-in-one: opened charge-transfer channel, positively shifted oxidation potential, and enhanced visible light response of g-C<sub>3</sub>N<sub>4</sub> photocatalyst through K and S Co-doping, *Int. J. Hydrog. Energ.* 45 (2020) 4534–4544, <https://doi.org/10.1016/j.ijhydene.2019.12.074>.
- [74] J. Li, B. Huang, Q. Guo, S. Guo, Z. Peng, J. Liu, Q. Tian, Y. Yang, Q. Xu, Z. Liu, B. Liu, Van der Waals heterojunction for selective visible-light-driven photocatalytic CO<sub>2</sub> reduction, *Appl. Catal. B: Environ.* 284 (2021), 119733, <https://doi.org/10.1016/j.apcatb.2020.119733>.
- [75] H. Niu, Z. Zhang, X. Wang, X. Wan, C. Shao, Y. Guo, Theoretical Insights into the mechanism of selective nitrate-to-ammonia electroreduction on single-atom catalysts, *Adv. Funct. Mater.* 31 (2020), 2008533, <https://doi.org/10.1002/adfm.202008533>.
- [76] H. Dong, Y. Zuo, N. Song, S. Hong, M. Xiao, D. Zhu, J. Sun, G. Chen, C. Li, Bimetallic synergetic regulating effect on electronic structure in cobalt/vanadium co-doped carbon nitride for boosting photocatalytic performance, *Appl. Catal. B: Environ.* 287 (2021), 119954, <https://doi.org/10.1016/j.apcatb.2021.119954>.
- [77] H. Wu, C. Li, H. Che, H. Hu, W. Hu, C. Liu, J. Ai, H. Dong, Decoration of mesoporous Co<sub>3</sub>O<sub>4</sub> nanospheres assembled by monocrystal nanodots on g-C<sub>3</sub>N<sub>4</sub> to construct Z-scheme system for improving photocatalytic performance, *Appl. Surf. Sci.* 440 (2018) 308–319, <https://doi.org/10.1016/j.apsusc.2018.01.134>.
- [78] Z. Xie, Y. Feng, F. Wang, D. Chen, Q. Zhang, Y. Zeng, W. Lv, G. Liu, Construction of carbon dots modified MoO<sub>3</sub>/g-C<sub>3</sub>N<sub>4</sub> Z-scheme photocatalyst with enhanced visible-light photocatalytic activity for the degradation of tetracycline, *Appl. Catal. B: Environ.* 229 (2018) 96–104, <https://doi.org/10.1016/j.apcatb.2018.02.011>.
- [79] J. Zheng, L. Zhang, Designing 3D magnetic peony flower-like cobalt oxides/g-C<sub>3</sub>N<sub>4</sub> dual Z-scheme photocatalyst for remarkably enhanced sunlight driven photocatalytic redox activity, *Chem. Eng. J.* 369 (2019) 947–956, <https://doi.org/10.1016/j.cej.2019.03.131>.
- [80] W. Wang, Z. Zeng, G. Zeng, C. Zhang, R. Xiao, C. Zhou, W. Xiong, Y. Yang, L. Lei, Y. Liu, D. Huang, M. Cheng, Y. Yang, Y. Fu, H. Luo, Y. Zhou, Sulfur doped carbon quantum dots loaded hollow tubular g-C<sub>3</sub>N<sub>4</sub> as novel photocatalyst for destruction of Escherichia coli and tetracycline degradation under visible light, *Chem. Eng. J.* 378 (2019), 122132, <https://doi.org/10.1016/j.cej.2019.122132>.
- [81] W. Wang, Q. Niu, G. Zeng, C. Zhang, D. Huang, B. Shao, C. Zhou, Y. Yang, Y. Liu, H. Guo, W. Xiong, L. Lei, S. Liu, H. Yi, S. Chen, X. Tang, 1D porous tubular g-C<sub>3</sub>N<sub>4</sub> capture black phosphorus quantum dots as 1D/0D metal-free photocatalysts for oxytetracycline hydrochloride degradation and hexavalent chromium reduction, *Appl. Catal. B: Environ.* 273 (2020), 119051, <https://doi.org/10.1016/j.apcatb.2020.119051>.
- [82] T. Pan, D. Chen, W. Xu, J. Fang, S. Wu, Z. Liu, K. Wu, Z. Fang, Anionic polyacrylamide-assisted construction of thin <sup>2</sup>D-<sup>2</sup>D WO<sub>3</sub>/g-C<sub>3</sub>N<sub>4</sub> Step-scheme heterojunction for enhanced tetracycline degradation under visible light irradiation, *J. Hazard. Mater.* 393 (2020), 122366, <https://doi.org/10.1016/j.jhazmat.2020.122366>.
- [83] H. Guo, C. Niu, C. Feng, C. Liang, L. Zhang, X. Wen, Y. Yang, H. Liu, L. Li, L. Lin, Steering exciton dissociation and charge migration in green synthetic oxygen-substituted ultrathin porous graphitic carbon nitride for boosted photocatalytic reactive oxygen species generation, *Chem. Eng. J.* 385 (2020), 123919, <https://doi.org/10.1016/j.cej.2019.123919>.
- [84] Y. Liang, W. Xu, J. Fang, Z. Liu, D. Chen, T. Pan, Y. Yu, Z. Fang, Highly dispersed bismuth oxide quantum dots/graphite carbon nitride nanosheets heterojunctions for visible light photocatalytic redox degradation of environmental pollutants, *Appl. Catal. B: Environ.* 295 (2021), 120279, <https://doi.org/10.1016/j.apcatb.2021.120279>.
- [85] W. Zhao, Y. Li, P. Zhao, L. Zhang, B. Dai, J. Xu, H. Huang, Y. He, D.Y.C. Leung, Novel Z-scheme Ag-C<sub>3</sub>N<sub>4</sub>/SnS<sub>2</sub> plasmonic heterojunction photocatalyst for degradation of tetracycline and H<sub>2</sub> production, *Chem. Eng. J.* 405 (2021), 126555, <https://doi.org/10.1016/j.cej.2020.126555>.